

Training-time Neuron Alignment through Permutation Subspace for Improving Linear Mode Connectivity and Model Fusion

Zexi Li¹ Zhiqi Li² Jie Lin¹ Tao Shen¹ Tao Lin³ Chao Wu¹

Abstract

In deep learning, stochastic gradient descent often yields functionally similar yet widely scattered solutions in the weight space even under the same initialization, causing barriers in the Linear Mode Connectivity (LMC) landscape. Overcoming these barriers is crucial for understanding deep learning dynamics and enhancing model-fusion algorithms. Previous studies highlight the role of *permutation symmetry* in reducing post-training barriers through network permutation. However, these post-hoc methods, demanding extra computations, are less effective for larger, complex models (e.g., ViT, LLM) due to numerous permutation matrices. Thus, in this paper, we study training-time neuron alignment. Our hypothesis suggests that training-time *permutation subspace* can reduce LMC barriers for free. We find that pruning at initialization supports this. Beyond pruning, we introduce TNA-PFN, a simple yet lossless algorithm using a partial gradient mask during training. TNA-PFN is theoretically and empirically validated for reducing LMC barriers. It excels in wide model fusion applications, especially in federated learning, where two algorithms based on TNA-FPN, named FedPFN and FedPNU, are proposed to show its prospects even under heterogeneous datasets. Moreover, TNA-PFN can enhance the generalization of model soup (Wortsman et al., 2022) for vision transformers and Cold fusion (Don-Yehiya et al., 2023) for pretrained language models.

1. Introduction

Understanding the loss landscape of Deep Neural Networks (DNNs) is the key to understanding the mechanisms

¹Zhejiang University, China. Zexi Li <zexi.li@zju.edu.cn>. ²Georgia Institute of Technology, USA. ³Westlake University, China. Correspondence to: Chao Wu <chao.wu@zju.edu.cn>, Tao Lin <lintao@westlake.edu.cn>.

Preprint.

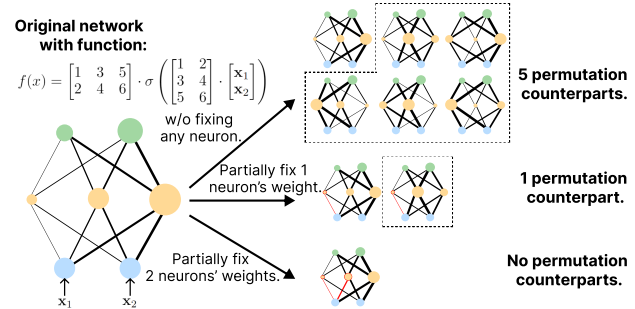


Figure 1: **A simple demonstration of reducing permutation symmetries.** There are 6 networks (1 original + 5 counterparts) which are functionally identical but with different permutations. The number of permutation symmetries can be reduced by asymmetrically fixing some weights (in red). Though this demonstration presents a simple static network permutation, we will show in the main paper that this kind of method can realize better neuron alignment under training dynamics.

and training dynamics behind generalization and optimization (Li et al., 2018b; Fort & Jastrzebski, 2019; Simsek et al., 2021; Vlaar & Frankle, 2022), and it is still an open problem. Empirical findings demonstrate that Stochastic Gradient Descent (SGD) will find many minima that are functionally similar but far away from each other in parameter space (Draxler et al., 2018; Zhang et al., 2021; Entezari et al., 2022). The literature in Linear Mode Connectivity (LMC) suggests that if we linearly interpolate two independently trained networks, which have the same initialization and trainset but have different SGD random seeds (i.e., batch orders), there will be a loss barrier in the landscape (Draxler et al., 2018; Garipov et al., 2018; Ainsworth et al., 2022) (also see Figure 3). The loss barrier reflects that the two SGD solutions fall into two different loss basins that cannot be linearly connected, and it is detrimental to model fusion (Ainsworth et al., 2022; Li et al., 2022).

The reasons behind the barrier in LMC are mainly the over-parameterization and permutation symmetry (also known as permutation invariance) properties of DNNs. Over-parameterization explains why there are abundant minima found by SGD (Zhang et al., 2021; Neyshabur et al., 2017; Safran & Shamir, 2018). Permutation symmetry suggests that the function of the network can remain the same while changing the permutations of neurons, which can result in many functionally same but geometrically different solu-

tions (Ainsworth et al., 2022; Wang et al., 2020a; Tatro et al., 2020). Previous works seek to achieve neuron alignment for improving LMC by utilizing the permutation symmetry property after training. In Entezari et al. (2022), it is conjectured that if taking all permutations into account, all SGD solutions can be mapped into the same loss basin where no barrier in LMC. Git Re-Basin (Ainsworth et al., 2022) further validates this conjecture by proposing three algorithms to find such permutations.

However, post-hoc neuron alignment is a hard combinatorial optimization problem. As stated in (Ainsworth et al., 2022), even for a three-layer MLP with 512 widths, the number of permutation symmetries is nearly 10^{3498} . When comes to larger foundation models, especially vision transformers (Dosovitskiy et al., 2021) and large language models (Radford et al., 2018), finding such an appropriate permutation to align neurons is more challenging and expensive. For the scenarios where alignment and fusion among multiple models are needed, especially federated learning (Wang et al., 2020b), the cost of the post-hoc alignment methods increases as the number of models.

Can we realize training-time neuron alignment?

If training-time alignment is reached, it will relieve the cost and necessity of post-matching. Also, when the model size and the number of models grow, the training-time method can boost model fusion for free without growing computations. In this paper, we hypothesize the key is to **break permutation symmetry** via **permutation asymmetry subspace**. During training, if the potential permutation symmetries are reduced, the neurons will be more aligned in a subspace so that the LMC barriers will decrease and model fusion will improve. A simple demonstration of how permutation asymmetry subspace works is in Figure 1.

We find that pruning at initialization supports our hypothesis. To overcome the limitations of pruning, we introduce TNA-PFN, a simple yet lossless algorithm using a partial gradient mask during training, which is then theoretically and empirically validated for reducing LMC barriers. TNA-PFN excels in wide model fusion applications, including in federated learning under heterogeneous datasets, model soup (Wortsman et al., 2022) for vision transformers, and CoLD fusion (Don-Yehiya et al., 2023) for pretrained language models. In a nutshell, we have the following **contributions**.

- We discover the neuron alignment problem from the perspective of training time, which provides new insights. We hypothesize that learning in *permutation subspaces* can reach better LMC.
- Under the hypothesis, we first find pruning at initialization can improve LMC. Then, we propose a simple yet more lossless training-alignment method TNA-PFN, which is validated under both theoretical and empirical analysis.
- TNA-PFN excels in wide model fusion applications. We extend TNA-PFN in federated learning and devise two algorithms, FedPFN and FedPNU. Also, TNA-PFN can

boost model soup and CoLD fusion for free, showcasing its prospects for pretrained foundation models.

2. Background and Related Works

In this section, we provide the basic backgrounds and definitions regarding linear mode connectivity and permutation invariance. Additionally, the preliminary of federated learning is in Appendix D.

Linear mode connectivity. In this paper, we focus on the linear mode connectivity of two SGD solutions, which have the same initialization but different data orders¹. We present the definitions of loss barrier and accuracy barrier below.

Definition 2.1. (Loss barrier (Entezari et al., 2022)) Let $f_{\mathbf{w}}(\cdot)$ be a function represented by a neural network with parameter vector \mathbf{w} that includes all parameters and $\mathcal{L}(\mathbf{w})$ be the any given loss (e.g., train or test error) of $f_{\mathbf{w}}(\cdot)$. Given two independently trained networks \mathbf{w}_1 and \mathbf{w}_2 , let $\mathcal{L}(\alpha\mathbf{w}_1 + (1 - \alpha)\mathbf{w}_2)$, for $\alpha \in [0, 1]$ be the loss of the linearly interpolated network. The loss barrier $B_{loss}(\mathbf{w}_1, \mathbf{w}_2)$ along the linear path between \mathbf{w}_1 and \mathbf{w}_2 is defined as the highest difference between the loss of the interpolated network and linear interpolation of the loss values of the two networks:

$$B_{loss}(\mathbf{w}_1, \mathbf{w}_2) = \sup_{\alpha} \{[\mathcal{L}(\alpha\mathbf{w}_1 + (1 - \alpha)\mathbf{w}_2)] - [\alpha\mathcal{L}(\mathbf{w}_1) + (1 - \alpha)\mathcal{L}(\mathbf{w}_2)]\}. \quad (1)$$

The loss barrier of the above definition is not bounded. To better depict and compare the barrier changes, we then propose a definition of the accuracy barrier which is bounded within $[0, 1]$.

Definition 2.2. (Accuracy barrier) Let $\mathcal{A}(\mathbf{w})$ be the accuracy (e.g., train or test accuracy) of $f_{\mathbf{w}}(\cdot)$. Let $\mathcal{A}(\alpha\mathbf{w}_1 + (1 - \alpha)\mathbf{w}_2)$, for $\alpha \in [0, 1]$ be the accuracy of the linearly interpolated network. The accuracy barrier $B_{acc}(\mathbf{w}_1, \mathbf{w}_2)$ along the linear path between \mathbf{w}_1 and \mathbf{w}_2 is defined as the highest ratio of the interpolated network’s accuracy drop to the averaged accuracy:

$$B_{acc}(\mathbf{w}_1, \mathbf{w}_2) = \sup_{\alpha} \left[1 - \frac{\mathcal{A}(\alpha\mathbf{w}_1 + (1 - \alpha)\mathbf{w}_2)}{\alpha\mathcal{A}(\mathbf{w}_1) + (1 - \alpha)\mathcal{A}(\mathbf{w}_2)} \right]. \quad (2)$$

The above definition maps the barrier into $[0, 1]$. If the accuracy barrier is 0, it means no barrier exists along the linear interpolation path; else if the barrier is nearly 1, it means the generalization of the interpolated model is nearly zero, and its prediction is no better than random guessing.

¹We note that there are other forms of LMC, such as the LMC from the initialization and the trained model (Vlaar & Frankle, 2022), and the LMC between two models with different initializations (Entezari et al., 2022). While in this paper, we focus on LMC and model fusion with specific applications in federated learning, we only consider the LMC cases with the same initialization.

Permutation invariance. Permutation invariance refers to the property that the positions (i.e., permutations) of neurons of a given network can be changed without changing the network’s function, and it is also known as permutation symmetry (Ainsworth et al., 2022). We take a multi-layer MLP as an example to demonstrate the property.

Assume an MLP network has $L + 1$ layers (containing input and output layer), and each layer contains J_l neurons, where $l \in \{0, 1, \dots, L\}$ is the layer index. J_0 and J_L are input and output dimensions. We denote the parameters of each layer as the weight matrix $\mathbf{W}_l \in \mathbb{R}^{J_l \times J_{l-1}}$ and the bias vector $\mathbf{b}_l \in \mathbb{R}^{J_l}$, $l \in \{1, 2, \dots, L\}$. The input layer does not have parameters. We use $\mathbf{h}_l \in \mathbb{R}^{J_l}$ as the outputs of the l -th layer. We have $\mathbf{h}_l = \sigma_l(\mathbf{W}_l \mathbf{h}_{l-1} + \mathbf{b}_l)$, where $\sigma_l(\cdot)$ is the element-wise activation function, e.g., ReLU. We use $\mathbf{\Pi} \in \{0, 1\}^{J \times J}$ as a permutation matrix that satisfies $\sum_j \mathbf{\Pi}_{\cdot, j} = 1$ and $\sum_j \mathbf{\Pi}_{j, \cdot} = 1$. By applying the permutation matrices to the layers, the network function remains unchanged. For the l -th layer, the layer-wise permutation process is

$$\mathbf{h}_l = \sigma_l(\mathbf{\Pi}_l \mathbf{W}_l \mathbf{\Pi}_{l-1}^T \mathbf{h}_{l-1} + \mathbf{\Pi}_l \mathbf{b}_l), \quad (3)$$

where $\mathbf{\Pi}_0 = \mathbf{I}$ and $\mathbf{\Pi}_L = \mathbf{I}$, meaning that the input and output are not shuffled. We note that the permutation matrices have the following properties:

$$\begin{aligned} \mathbf{\Pi}^T \mathbf{\Pi} &= \mathbf{I}, \mathbf{\Pi} \mathbf{a} + \mathbf{\Pi} \mathbf{b} = \mathbf{\Pi}(\mathbf{a} + \mathbf{b}), \\ \mathbf{\Pi} \mathbf{a} \odot \mathbf{\Pi} \mathbf{b} &= \mathbf{\Pi}(\mathbf{a} \odot \mathbf{b}), \sigma(\mathbf{\Pi} \mathbf{x}) = \mathbf{\Pi} \sigma(\mathbf{x}), \end{aligned} \quad (4)$$

where \mathbf{I} is the identity matrix, \odot denotes Hadamard product, and $\sigma(\cdot)$ is an element-wise function.

The connection between LMC and permutation invariance. In Entezari et al. (2022); Ainsworth et al. (2022), it is conjectured that if applying appropriate permutation matrices to the networks, two SGD solutions that have barriers before can be mapped into the same loss basin and linearly connected (with low barriers). In previous literature, post-hoc matching methods are proposed to approximate the right permutations (Ainsworth et al., 2022; Peña et al., 2023).

The comparison between our paper and Frankle et al. (2020). In Frankle et al. (2020), the authors find that better LMC will result in better results of the lottery ticket hypothesis (a kind of pruning). However, their conclusions cannot infer that pruning will result in better LMC, where our contributions lie (see more detailed discussions in Appendix E). It is noteworthy that we are the first to present this finding and it is non-trivial.

We include detailed related works in Appendix E.

3. Permutation Subspace and Linear Mode Connectivity

3.1. Hypothesis and Preliminary Finding

Previous works find that permutation symmetry is the main cause of LMC barriers. Due to the numerous parameters

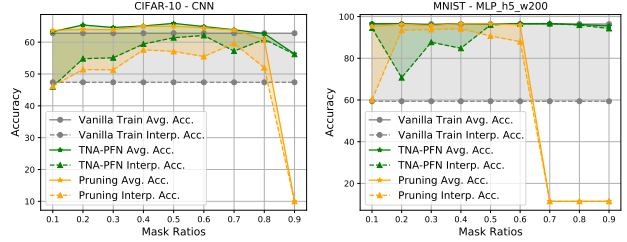


Figure 2: **LMC of random pruning at initialization and TNA-PFN under different mask ratios.** For pruning, the mask ratio is the pruning ratio. “Avg. Acc.” means averaged accuracies of individual models, and “Interp. Acc.” means the accuracy of the interpolated model ($\alpha = 0.5$) of two modes. The shadow areas mean the accuracy barriers in LMC, the smaller the better.

and permutation symmetries, SGD will find solutions far from each other in the landscapes during training. Therefore, we think a possible solution for training-time neuron alignment is breaking permutation symmetries in training via the same asymmetric subspace across models, so we make the following hypothesis.

Hypothesis 3.1 (Informal). If we can reduce the potential number of permutation symmetries by learning different models in the same permutation subspace, the linear mode connectivity will be improved.

Network pruning improves LMC. One straight-forward method which fits Hypothesis 3.1 is network pruning at initialization. We apply random weight pruning to an initialized model, and different neurons will have different pruning structures (i.e., pruning ratios and pruning positions), so the symmetric structure of the network is broken, and the permutations of neurons are limited. From this pruned initialization, different training runs will learn in the same subspace where pruned weights are always zeros and permutations of neurons are constrained.

It is validated in Figure 2 that pruning can actually improve LMC compared with vanilla training, which supports our hypothesis. But when the pruning ratio ρ is high (i.e., 0.8 and 0.9), pruning will result in an untrainable network with nearly zero generalization. It is more severe when the initialized model is pretrained transformers, from Figure 14, it can be seen that even if the pruning ratio is mild ($\rho = 0.2$), random pruning is fatal to ViT’s network generalization. Thus, to overcome pruning’s drawbacks, we propose a simple yet lossless (in terms of generalization) training-time alignment method in subsection 3.2.

3.2. Training-time Neuron Alignment with Partially Fixed Neurons

3.2.1. METHOD FORMULATION

Instead of setting the weights as zeros like pruning, we propose to fix some neurons’ weights, which will also break

the network symmetry to reduce the permutations while preserving the expressiveness power of networks. An intuitive demonstration is in [Figure 1](#), by fixing some weights of neurons, the number of potential permutations decreases. Specifically, given an initial network parameterized by a weight vector $\mathbf{w}^0 \in \mathbb{R}^d$. For \mathbf{w}^0 , we randomly generate a mask for each layer according to the mask ratio ρ (refers to the proportion of zeros in the mask \mathbf{m}^0), and the whole mask is $\mathbf{m}^0 \in \{0, 1\}^d$. In \mathbf{m}^0 , 0 for fixed and 1 for updated, indicating the parameter update status. We individually train n models with different batch orders or datasets. We set each model’s initialization as $\mathbf{w}_i \leftarrow \mathbf{w}^0, i \in [n]$. Each model $\mathbf{w}_i, i \in [n]$ conducts the following updates in every SGD iteration:

$$\mathbf{w}_i \leftarrow \mathbf{w}_i - \eta(\mathbf{m}^0 \odot \mathbf{g}_i(\mathbf{w}_i)), \quad (5)$$

where \odot denotes the element-wise Hadamard product, η refers to the learning rate, and \mathbf{g}_i is its gradients of the optimizer, such as SGD or Adam. After training for E epochs, we validate the LMC with respect to the loss or accuracy barriers in [Definitions 2.1](#) and [2.2](#). The method is notated as TNA-PFN.

We also present how TNA-PFN improves LMC under different ρ in [Figure 2](#), which shows TNA-PFN’s effectiveness in reducing the barriers and its advantages over pruning. Additionally, a *connectivity-accuracy tradeoff* is observed for both TNA-PFN and pruning that when the mask ratio is higher, the accuracy barriers diminish along with the decrease in the averaged accuracies of independently trained models. However, when ρ is set appropriately (e.g., 0.4-0.6 for the CIFAR-10 and CNN setting), both the averaged accuracy and LMC can be improved.

Discussions on differences between TNA-PFN and previous gradient-mask-based methods. Applying gradient masks is discovered in previous gradient compression literature of distribution optimization, but our method is different from the previous works in the aspects as follows. **Motivation difference:** Gradient compression is proposed for communication efficiency of distributed optimization while we study the training-time neuron alignment problem in LMC. **Implementation difference:** Gradient compression uses *different* random top-k gradient masks at each worker and *changes the mask per communication iteration* ([Lin et al., 2018](#); [Vogels et al., 2019](#)); whereas, TNA-PFN uses *the same* random gradient masks at each model, *fixes the mask*, and independently trains the models *without any communications*; and FedPFN/FedPNU (presented in [subsection 4.2](#)) uses *the same* masks at each client’s local training and changes the mask *per global communication round*. **Effect difference:** Since the masks of workers are different and changing, previous gradient compression methods cannot learn in a consistent subspace of parameters, while we learn in a subspace by the same gradient mask so that some neuron weights are not updated.

3.2.2. THEORETICAL ANALYSIS

We make a theoretical analysis about how TNA-PFN can improve LMC, shown in [Theorem 3.2](#) (proof is in [Appendix B](#)). The main idea is to treat the linear interpolated landscape of the barrier as a function of parameter α , and the connectivity can be depicted by the first and second derivatives of the function.

Theorem 3.2. *We define a two-layer neural network with ReLU activation, and the function is $f_{\mathbf{v}, \mathbf{U}}(\mathbf{x}) = \mathbf{v}^\top \sigma(\mathbf{U}\mathbf{x})$ where $\sigma(\cdot)$ is the ReLU activation function. $\mathbf{v} \in \mathbb{R}^h$ and $\mathbf{U} \in \mathbb{R}^{h \times d}$ are parameters² and $\mathbf{x} \in \mathbb{R}^d$ is the input which is taken from $\mathbb{X} = \{\mathbf{x} \in \mathbb{R}^d \mid \|\mathbf{x}\|_2 < b\}$ uniformly. Consider two different networks parameterized with $\{\mathbf{U}, \mathbf{v}\}$ and $\{\mathbf{U}', \mathbf{v}'\}$ respectively, and for arbitrarily chosen masks $\mathbf{M}_{\mathbf{v}} \in \{0, 1\}^h$ and $\mathbf{M}_{\mathbf{U}} \in \{0, 1\}^{h \times d}$, each element of \mathbf{U} and \mathbf{U}' , \mathbf{v} and \mathbf{v}' is i.i.d. sampled from a sub-Gaussian distribution sub-G(0, $\sigma_{\mathbf{v}}^2$) and sub-G(0, $\sigma_{\mathbf{U}}^2$) respectively with setting $v_i = v'_i$ when $M_{\mathbf{v}, i} = 0$ and $U_{i,j} = U'_{i,j}$ when $M_{\mathbf{U}, ij} = 0$. We consider the linear mode connectivity of the two networks and define the difference function between interpolated network and original networks as $z_{\mathbf{x}}(\alpha) = (\alpha\mathbf{v} + (1-\alpha)\mathbf{v}')^\top \sigma((\alpha\mathbf{U} + (1-\alpha)\mathbf{U}')\mathbf{x}) - \alpha\mathbf{v}^\top \sigma(\mathbf{U}\mathbf{x}) - (1-\alpha)\mathbf{v}'^\top \sigma(\mathbf{U}'\mathbf{x})$, $\alpha \in [0, 1]$. The function over all inputs is defined as $z(\alpha) = \frac{1}{|\mathbb{X}|} \int_{\mathbb{X}} z_{\mathbf{x}}(\alpha) d\mathbf{x}$. We use $|z(\alpha)|$, $\left| \frac{dz(\alpha)}{d\alpha} \right|$ and $\left| \frac{d^2z(\alpha)}{d\alpha^2} \right|$ to depict the linear mode connectivity, showing the output changes along the α path. With probability $1 - \delta$, it has,*

$$|z(\alpha)| \leq \sqrt{2}b\sigma_{\mathbf{v}}\sigma_{\mathbf{U}} \log(8h/\delta) \sqrt{h} \sqrt{1 - \rho_{\mathbf{U}}}, \quad (6)$$

$$\left| \frac{dz(\alpha)}{d\alpha} \right| \leq 4\sqrt{2}b\sigma_{\mathbf{v}}\sigma_{\mathbf{U}} \log(24h/\delta) \sqrt{h} (\sqrt{1 - \rho_{\mathbf{v}}} + \sqrt{1 - \rho_{\mathbf{U}}}), \quad (7)$$

$$\left| \frac{d^2z(\alpha)}{d\alpha^2} \right| \leq 8b\sigma_{\mathbf{v}}\sigma_{\mathbf{U}} \log(4h/\delta) \sqrt{h} \sqrt{(1 - \max\{\rho_{\mathbf{U}}, \rho_{\mathbf{v}}\})}, \quad (8)$$

where $\rho_{\mathbf{v}}$ and $\rho_{\mathbf{U}}$ refer to the mask ratios (the proportion of zeros in the mask) of masks $\mathbf{M}_{\mathbf{v}}$ and $\mathbf{M}_{\mathbf{U}}$ respectively.

Remark 3.3. $|z(\alpha)|$ is the barrier given α . $\left| \frac{dz(\alpha)}{d\alpha} \right|$ demonstrates the barrier function changes along the interpolation path $\alpha \in [0, 1]$, and the smaller value means smaller changes. If $\left| \frac{dz(\alpha)}{d\alpha} \right| \rightarrow 0$, it means that $z(\alpha)$ is a constant, but it does not mean $z(\alpha)$ is a linear function of α . $\left| \frac{d^2z(\alpha)}{d\alpha^2} \right|$ reflects the linearity of function $z(\alpha)$, and if $\left| \frac{d^2z(\alpha)}{d\alpha^2} \right| \rightarrow 0$, it means that $z(\alpha)$ is linear w.r.t. α .

[Theorem 3.2](#) shows how TNA-PFN improves LMC by masking some weights from updating (setting $\rho_{\mathbf{v}}$ and $\rho_{\mathbf{U}}$ larger than zeros), where the networks learn in a unified permutation subspace.

²For simplicity and without loss of generality, the bias terms are omitted.

Table 1: The performances of post-matching methods after TNA-PFN. Interpolated Accuracy (Interp. Acc.) means the accuracy of the linearly interpolated model, i.e., $\mathcal{A}(0.5\mathbf{w}_1 + 0.5\mathbf{w}_2)$. ‘‘Iter.’’ refers to the number of iterations in the post-matching methods, reflecting the computation costs.

Metrics\Methods	CIFAR-10				MNIST			
	MLP_h2_w200		ResNet20		MLP_h5_w200		MLP_h6_w200	
	Vanilla train	TNA-PFN	Vanilla train	TNA-PFN	Vanilla train	TNA-PFN	Vanilla train	TNA-PFN
Interp. Acc. w/o Post-matching	31.9±2.4	43.7±0.4	36.1±4.3	46.2±4.7	59.4±24.2	84.8±8.2	63.7±15.6	87.5±8.9
Interp. Acc. after 10 Iter. of SA	32.2±2.2	43.7±0.4	36.7±3.4	46.2±4.7	59.7±24.2	85.4±8.0	64.9±14.4	87.7±9.1
Interp. Acc. after 100 Iter. of SA	31.9±2.4	43.7±0.4	36.1±4.3	46.2±4.7	60±24.1	86.9±7.6	64.2±15.1	88.2±7.9
Interp. Acc. after WM	44.7±1.3	48.5±0.9	53.7±2.9	53.6±2.5	96.9±0.3	97.1±0.2	96.8±0.3	96.9±0.4
Required Iter. in WM	5.2±1.0	4.8±1.5	4.6±0.5	2.5±0.2	10.4±1.2	7.6±3.8	11.2±1.8	7.33±4.2

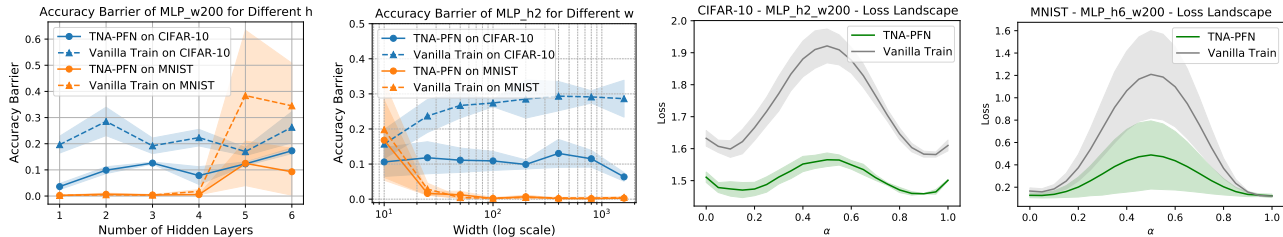


Figure 3: Left two: Accuracy barriers of MLP under different hidden layers (h) and widths (w). Right two: Loss landscapes of MLP. For MLPs, if the barriers exist, TNA-PFN can reduce them. The shadow areas refer to the standard deviations.

3.2.3. EMPIRICAL RESULTS ON LINEAR MODE CONNECTIVITY

In this subsection, we will conduct experiments to validate the effectiveness of TNA-PFN in improving LMC. If not mentioned otherwise, the mask ratio ρ of TNA-PFN is 0.4 (the hyperparameter which is mild across various settings).

Different model depths, widths, and architectures.

In Figure 3, we conduct experiments on MLP with different hidden layers and widths. For MNIST (LeCun & Cortes, 2010), we find shallower and wider networks will not cause barriers, which is consistent with the previous observations (Entezari et al., 2022). For CIFAR-10 (Krizhevsky et al., 2009), the barriers always exist under various depths and widths. Our proposed TNA-PFN can obviously reduce the accuracy barriers from 0.3-0.4 to 0.1, and we also visualize the loss landscapes, which illustrate the barrier reductions. To see more results and illustrations, please refer to subsection C.1.

We study the LMC of simple CNN and ResNets and present the results in Figure 4. ResNets (He et al., 2016) have higher barriers than simple CNN, and the barriers are exacerbated when the networks are deeper or wider. It is suggested that TNA-PFN can lower the barriers under

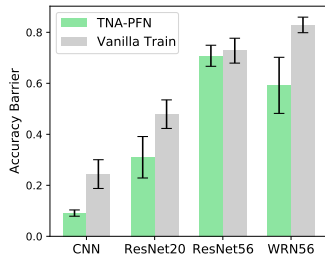


Figure 4: Accuracy barriers under different model architecture. WRN56 abbreviates for WideResNet56. CIFAR-10.

different architectures.

Generally, we observe that TNA-PFN has more dominant advantages when the models are wider, and the observations are: (1) the second figure in Figure 3: for CIFAR-10 when width increases, the barriers of vanilla training go up while the barriers of TNA-PFN go down; (2) Figure 4: the barrier reduction of TNA-PFN is more obvious for WRN56 compared with ResNet56. This observation is consistent with previous literature about permutation symmetry and linear mode connectivity (Entezari et al., 2022).

The role of post-hoc neuron alignment methods after training-time alignment. We consider simulated annealing (SA) (Entezari et al., 2022) and weight matching (WM) (Ainsworth et al., 2022) after TNA-PFN in Table 1. SA requires large computations, and we notice the improvements are also marginal. Under limited computation budgets (10 or 100 iterations), we find that TNA-PFN can reach a higher result than vanilla training after SA. For WM, it is indicated that after TNA-PFN, the required iterations are shortened while the interpolated accuracies are similar. The results reveal that training-time neuron alignment can reduce the costs of post-matching and remain similar or even better post-matched LMC.

More deep learning tasks. We conduct more experiments beyond vision tasks and display the results in Table 4. **Polynomial approximation task** (Peña et al., 2023; von Oswald et al., 2019): we use an MLP with one hidden layer to approximate the second and third polynomial functions: $y = 2x^2 - 1, y = (x - 3)^3$. **Sentiment analysis of text** (Liu et al., 2022b): we use an LSTM (Graves & Graves, 2012) to predict the sentiment of IMDb reviews (Maas et al., 2011). It can be seen that the loss barriers are decreased by training-

Table 2: **Linear mode connectivity of non-random initializations.** Dataset: CIFAR-10. *Semi-trained CNN*: The initialization is first trained on a disjoint subset of CIFAR-10 for 0.5 epoch. *Pretrained ResNet18*: Pretrained on ImageNet.

Models	Metrics	Vanilla Train	TNA-PFN
Semi-trained CNN	Avg. Acc.	64.4±0.7	65.8±0.2
	Interp. Acc.	52.8±2.3	63.3±1.2
	Acc. Barrier	0.181±0.027	0.0413±0.018
	Loss Barrier	0.306±0.058	0.0762±0.038
Pretrained ResNet18	Avg. Acc.	65.3±1.2	69.1±0.5
	Interp. Acc.	11.9±0.39	54.9±8.2
	Acc. Barrier	0.817±0.003	0.205±0.12
	Loss Barrier	0.957±0.45	0.395±0.2

Table 3: **Linear mode connectivity of multi-model fusion.** The number of models is 5.

Datasets / Models	Metrics	Vanilla Train	TNA-PFN
CIFAR-10 / CNN	Avg. Acc.	63.1±0.6	65.5±0.3
	Interp. Acc.	21.3±9.1	48.3±7.2
	Acc. Barrier	0.663±0.14	0.264±0.11
CIFAR-10 / MLP_h2_w200	Avg. Acc.	44.2±0.5	48.4±0.5
	Interp. Acc.	21.6±1.9	36.6±1.4
	Acc. Barrier	0.511±0.043	0.245±0.035
	Loss Barrier	0.511±0.043	0.245±0.035
MNIST / MLP_h5_w200	Avg. Acc.	96.5±0.3	96.5±0.2
	Interp. Acc.	34.5±15.5	87.1±9.4
	Acc. Barrier	0.643±0.16	0.0974±0.096

Table 4: **Results of loss barriers on more deep learning tasks.**

Methods/Datasets	2nd Polynomial	3rd Polynomial	IMDb
Vanilla Train	0.268±0.061	0.0554±0.047	0.710±0.17
TNA-PFN	0.0381±0.0096	0.0355±0.023	0.375±0.17

time alignment under both polynomial approximation and sentiment analysis tasks. We also implement the experiments on a large-scale dataset, the subset of ImageNet (Deng et al., 2009; tin, Accessed: 2023). The result is shown in Table 10 of Appendix.

Results under non-random initializations. We also examine whether training-time alignment can help when the initializations are not random, which commonly occurs in the pretraining-finetuning paradigm and federated learning. As presented in Table 2, TNA-PFN is more advantageous to improve LMC under non-random initializations. TNA-PFN nearly clears the barriers under the setting of CNN and CIFAR-10. For the pretrained ResNet18, we observe that TNA-PFN reduces the barrier by a large margin while improving individual accuracies.

Layer-wise analysis. We conduct a layer-wise analysis of TNA-PFN to see which layer matters most in improving LMC in Figure 5 of Appendix.

4. Training-time Neuron Alignment Enables Wide Model Fusion Applications

In this section, we will showcase how training-time neuron alignment can facilitate wide model fusion applications. In subsection 4.1, we show TNA-PFN can improve LMC of multi-model fusion; in subsection 4.2, we present two algorithms in federated learning based on TNA-PFN and conduct extensive experiments; while in subsection 4.3, we validate TNA-PFN can boost the generalization of model soup (Wortsman et al., 2022) and CoLD fusion (Don-Yehiya et al., 2023) for pretrained transformers.

4.1. LMC of Multi-model Fusion

We study the LMC of multi-model fusion and the results are shown in Table 3. We consider the connectivity of 5 independently trained models by assigning a uniformly weighted

fusion after training. We test the generalization of the fused model as interpolated accuracy and compared it with the averaged accuracy of independent models. It is evident that after the training-time alignment, the interpolated accuracies are largely promoted by up to 152% and the barriers are much lower with a maximal reduction of 84.9%, showing TNA-PFN’s prospects in applications like federated learning. It is also intriguing to observe that the averaged accuracies also increase after TNA-PFN. We explain this phenomenon that partially fixing some weights may play the role of regularization and for some models with redundant neurons, this regularization can also help in generalization.

4.2. Federated Learning

Federated learning requires model fusion on the server, and it meets neuron alignment problems during training (Wang et al., 2020b; Li et al., 2022; Yurochkin et al., 2019). Previous methods utilize post-hoc matching methods on the server, and they usually require large computations. In this paper, we extend training-time neuron alignment methods in federated learning (FL) to improve the global model’s generalization to showcase its potential in applications. Due to the space limit, the preliminary of FL is in Appendix D.

4.2.1. METHODS

In this subsection, we propose two variants of TNA-PFN in FL, the first is called Federated Learning with Partially Fixed Neurons (FedPFN) and the second is Federated Learning with Progressive Neuron Updating (FedPNU).

FedPFN (pseudo-code in Algorithm 1). There are T communication rounds in FL. During FL training, in communication round $t \in [T]$, the central server generates a new random mask $\mathbf{m}^t \in \{0, 1\}^d$ according to the masking ratio ρ . Also, the central server generates the global model \mathbf{w}^t by the global aggregation scheme (e.g., FedAvg (McMahan et al., 2017)) and sends \mathbf{m}^t and \mathbf{w}^t to the clients.

Clients initialize their local models as the received global model, $\mathbf{w}_i^t \leftarrow \mathbf{w}^t$. Client i conducts SGD updates with mask \mathbf{m}^t , so that the masked neuron weights are fixed at

Table 5: **Top-1 test accuracy (%) achieved by comparing the FL methods on three datasets with different model architectures ($E = 5$). Bold fonts highlight the best two methods in each setting.**

Datasets	FashionMNIST				CIFAR-10				CIFAR-100			
	dir	100		0.1		100		0.1		100		0.1
Methods/Models	MLP	LeNet	MLP	LeNet	CNN	ResNet	CNN	ResNet	CNN	ResNet	CNN	ResNet
FedAvg	88.7±0.5	90.5±0.1	81.7±2.7	83.5±3.8	65.4±1.2	73.4±2.1	57.5±1.3	50.9±1.8	18.9±0.9	26.4±0.4	22.6±0.9	28.5±1.3
FedProx	88.0±0.1	90.0±0.2	82.6±0.9	85.8±0.7	65.4±0.9	65.5±0.8	59.7±1.1	49.9±2.1	27.7±0.5	26.7±0.4	24.7±0.0	23.0±1.5
FedDyn	88.2±0.2	85.3±7.7	65.2±0.4	68.9±5.7	33.2±1.6	19.2±1.2	20.5±2.1	19.0±0.9	23.7±4.7	18.6±1.1	21.1±0.9	1.0±0.0
FedRoD	87.9±1.3	89.9±0.4	81.7±1.4	85.5±1.2	64.4±0.8	74.0±1.4	58.6±1.5	52.2±1.3	20.3±0.5	26.4±0.9	19.5±0.5	26.5±0.5
FedNH	86.6±1.9	87.5±0.6	69.2±6.8	72.3±4.6	66.5±1.3	71.6±0.7	49.1±6.1	28.9±12.7	21.5±0.5	26.1±0.1	20.1±0.2	25.6±0.8
FedETF	88.3±0.4	89.9±0.3	81.9±1.1	85.7±1.3	65.0±1.0	71.8±0.4	53.6±0.9	59.8±2.4	22.1±0.2	28.4±0.7	20.1±0.4	27.7±0.5
FedDF	89.1±0.1	90.3±0.2	81.3±2.8	86.0±1.9	66.3±0.8	75.6±3.3	57.6±3.0	55.2±1.4	21.4±0.3	28.5±1.0	24.2±0.2	31.2±1.2
FedPFN	88.8±0.1	90.6±0.1	81.8±1.7	84.9±2.8	66.9±0.6	73.7±1.3	62.2±0.5	51.4±0.7	20.9±0.7	27.3±0.3	24.9±1.2	34.5±2.4
FedPNU	88.7±0.2	90.4±0.2	83.2±0.8	86.6±1.0	67.5±0.3	73.5±2.5	61.3±0.4	55.9±1.6	22.1±0.5	29.4±0.0	24.8±0.2	35.3±1.5
FedDF+FedPFN	88.9±0.2	90.5±0.1	80.7±3.3	86.4±2.0	67.9±0.4	73.0±1.2	59.3±3.6	54.4±5.1	27.8±0.8	31.0±1.3	27.0±0.2	31.1±1.2
FedDF+FedPNU	88.7±0.1	90.7±0.2	82.1±2.4	86.4±1.8	66.4±0.8	74.1±1.3	60.0±2.4	57.1±4.1	22.2±0.9	30.8±1.2	25.8±0.7	35.2±1.2

this round. The SGD updates are as follows for E epochs,

$$\mathbf{w}_i^t \leftarrow \mathbf{w}_i^t - \eta_l(\mathbf{m}^t \odot \mathbf{g}_i(\mathbf{w}_i^t)), \quad (9)$$

where \odot denotes the element-wise (Hadamard) product and η_l refers to the local learning rate. By applying FedPFN, during local training, all clients learn in the same effective permutation subspace so model drifts and permutation invariance issues can be relieved. Besides, the neuron mask \mathbf{m}^t changes from round to round, so all the neurons can be evenly trained, and it will break the connectivity-accuracy tradeoff observed in LMC (Figure 2).

FedPNU (pseudo-code in Algorithm 2). In FedPNU, we additionally consider a reversed mask $\hat{\mathbf{m}}^t$ of \mathbf{m}^t . During training, the clients first train with mask \mathbf{m}^t according to Equation 9 for the half local training, i.e., $\text{int}(\frac{E}{2})$ epochs; then, they train with the reversed mask $\hat{\mathbf{m}}^t$ for the remaining $E - \text{int}(\frac{E}{2})$ epochs. In FedPNU, the clients progressively train the networks in a subspace and the accordingly complementary subspace, by which the neurons of local models are more aligned.

For more discussion about the related works of subspace and partial training in federated learning, please refer to Appendix E.

We note that FedPFN and FedPNU are lightweight and flexible since they only add a gradient mask before the optimizer’s updates, so they are orthogonal to current FL algorithms (especially server-side global model fusion schemes). We will show they can be incorporated into existing FL methods for further improving performances.

4.2.2. EXPERIMENTS

Settings and baselines. We use three datasets to verify the algorithms: FashionMNIST (Xiao et al., 2017), CIFAR-10, and CIFAR-100 (Krizhevsky et al., 2009). We adopt the Dirichlet sampling to generate non-IID data (a.k.a., heterogeneous data) for each client, which is widely used in FL literature (Lin et al., 2020; Chen & Chao, 2022). The Dirichlet sampling considers a class-imbalanced data heterogeneity, controlled by the hyperparameter “dir”, the smaller, the

Table 6: **Results about different numbers of clients and partial selections.** CIFAR-10 with dir = 0.5, $E = 3$, CNN.

Methods	Number of clients (selection ratio)				
	30 (1.0)	60 (1.0)	90 (0.4)	90 (0.6)	90 (1.0)
FedAvg	63.6±1.2	62.5±0.7	60.8±0.4	61.4±0.7	61.6±0.5
FedPFN	65.6±0.1	64.7±0.3	62.9±0.4	63.6±0.5	64.0±0.4
FedPNU	65.2±0.2	63.2±0.7	62.0±0.9	62.3±0.3	62.3±0.7

more heterogeneous. We vary “dir” in range [100, 0.5, 0.1], which respectively means IID, moderately non-IID, and extremely non-IID data. For FashionMNIST, the models are MLP_h2_w200 and LeNet5 (LeCun et al., 1998); for CIFAR-10 and CIFAR-100, the models are simple CNN (Li et al., 2023a) and ResNet20 (He et al., 2016). We consider the state-of-the-art FL methods as the baselines. For client-side methods, we consider vanilla training, FedProx (Li et al., 2020a), FedDyn (Acar et al., 2020), FedRoD (Chen & Chao, 2022), FedNH (Dai et al., 2023), FedETF (Li et al., 2023b); for the server-side algorithms, we consider FedAvg (McMahan et al., 2017) and FedDF (Lin et al., 2020). If not mentioned otherwise, the number of clients in the experiments is 20 and full client selection is applied. For more implementation details, please refer to Appendix A.

Different datasets and models. In Table 5, we demonstrate the results under different datasets, data heterogeneity, and models. Since our methods are client-side algorithms, we note that the vanilla FedPFN/FedPNU are actually FedAvg+FedPFN/FedPNU, and we also combine our methods with the server-side approach FedDF, namely FedDF+FedPFN/FedPNU. *The results show that FedPFN and FedPNU consistently improve over FedAvg, showing that incorporating the training-time alignment method can boost model fusion in FL. Also, our methods can strengthen FedDF to reach a higher performance.* Generally, our methods and the variants incorporating FedDF always achieve state-of-the-art results across various settings.

Different number of clients. We scale the number of clients in the range [30, 60, 90] and apply partial client selections

Table 7: Results of random initialization pruning in FL and fixing FedPFN’s mask. CIFAR-10 with dir = 0.3 and $E = 3$.

Models\Methods	FedAvg	FedPFN	FedPFN (fixed)	FedPruning
CNN	64.8±1.0	65.7±1.0	64.9±1.0	63.7±1.1
ResNet20	72.0±0.7	72.4±0.5	71.3±1.3	70.2±1.3

Table 8: Results of model soup (Wortsman et al., 2022) for finetuning pretrained transformers. The initialized model is ViT-B/32 pretrained on CLIP. The number of models per experiment is 5. "Avg. Acc." refers to the averaged accuracy of individual models. "Diff_lr" ("Diff_seed") refers to model soup with different learning rates (random seeds).

Dataset / Type of Soup	Metrics	Vanilla Train	TNA-PFN
CIFAR-10 / Diff_lr	Avg. Acc.	80.3	79.9 (0.4↓)
	Uniform Soup	91.6	91.2 (0.4↓)
	Greedy Soup	96.7	96.9 (0.2↑)
CIFAR-10 / Diff_seed	Avg. Acc.	96.3	96.6 (0.3↑)
	Uniform Soup	97.4	97.6 (0.2↑)
	Greedy Soup	97.5	97.6 (0.1↑)
CIFAR-100 / Diff_lr	Avg. Acc.	55.5	56.6 (1.1↑)
	Uniform Soup	66.6	67.6 (1.0↑)
	Greedy Soup	80.9	82.6 (1.7↑)
CIFAR-100 / Diff_seed	Avg. Acc.	64.8	67.8 (3.0↑)
	Uniform Soup	62.1	67.2 (5.1↑)
	Greedy Soup	67.7	73.3 (5.6↑)

when the number is 90. From Table 6, it is found that our methods can still improve the global model’s generalization when scaling up the clients, which showcases the effectiveness of training-time neuron alignment methods in improving multi-model linear mode connectivity.

Comparison with pruning and fixed masks. We make an ablation study on the design of FedPFN. We compare FedPFN with the TNA-PFN variant denoted as FedPFN (fixed) in which we fix the neuron mask \mathbf{m}^t in every round ($\mathbf{m}^t = \mathbf{m}^{t-1} = \mathbf{m}^0$). We also implement the setting where the random pruning is applied at initialization before FL training, named as FedPruning. Table 7 presents the results. Although we find pruning can improve LMC in section 3, it will cause generalization degradation in FL due to the connectivity-accuracy tradeoff. Also, if we incorporate TNA-PFN by keeping the same neuron mask during FL training, it will have marginal or even negative improvements. The above findings indicate that FL is sensitive in the subspaces and further validate the rationale of our devised methods.

More experiments. We include more results and illustrations in subsection C.2, such as different local epochs experiments, and different mask ratios for FedPFN and FedPNU.

4.3. Model Soup and CoLD Fusion

We will show that TNA-PFN and its derived FedPFN and FedPNU can improve model fusion performances using more complex transformer-based models, under the pretraining-finetuning paradigm.

Model soup. Model soup is a model fusion technique for finetuning foundation models (Wortsman et al., 2022). It

Table 9: Results of CoLD fusion (Don-Yehiya et al., 2023) for pretrained language models. The model is RoBERTa-base and the three datasets are from GLUE (Wang et al., 2019). “Sum” refers to the joint testset combining the three datasets.

Methods	COLA	RTE	MRPC	Sum
FedAvg	77.66	82.31	77.33	77.66
FedAvg+TNA-PFN	80.73	83.75	81.86	81.43
FedPFN	82.74	85.56	81.16	82.66
FedPNU	81.50	83.39	79.48	80.11

incorporates finetuning several models from the same initialization under different hyperparameters and then greedily (greedy soup) or uniformly (uniform soup) fusing them into one for boosting the generalization on the finetuned task. In Table 8, we conduct model soup experiments using ViT-B/32 (Dosovitskiy et al., 2021) pretrained on CLIP (Radford et al., 2021). The results show greedy soup can realize the maximal generalization gain compared with uniform soup and vanilla training, which is consistent with the literature. *It demonstrates that TNA-PFN can consistently promote greedy soups’ generalization.* We also show the results of TNA-PFN using different mask ratios in Figure 14.

CoLD fusion. CoLD fusion is proposed to improve the pretrained language models’ multi-task generalization via collaborative model fusion (Don-Yehiya et al., 2023). The original procedure of CoLD fusion resembles FedAvg (McMahan et al., 2017), where models are trained on different task datasets, and iterative model fusion is conducted after several epochs. *The results are shown in Table 9, where three variants of TNA-PFN: FedAvg+TNA-PFN, FedPFN, and FedPNU all surpass vanilla FedAvg across all datasets.*

Notably, our TNA-PFN-based methods only apply a sparse gradient mask during training, which only adds little computation and is flexible and applicable across any model architecture. Compared with the post-hoc neuron alignment methods, our methods can boost the generalization of finetuning foundation models for free.

5. Conclusion

This paper focuses on training-time neuron alignment to enhance linear mode connectivity (LMC) and model fusion. We hypothesize that a training-time permutation subspace can reduce LMC barriers cost-free, which is corroborated by our findings with pruning at initialization. Advancing beyond pruning, we introduce TNA-PFN, a simple yet lossless algorithm that employs a partial gradient mask during training. TNA-PFN is validated both theoretically and empirically in reducing LMC barriers and shows strong performance in a wide range of model fusion applications, including federated learning, where we propose two algorithms based on TNA-PFN. Furthermore, TNA-PFN can enhance the generalization of model soup in vision transformers and CoLD fusion for pretrained language models.

Impact Statements

This paper presents work whose goal is to advance the field of Machine Learning. There are many potential societal consequences of our work, none of which we feel must be specifically highlighted here.

References

- Tiny imagenet. <https://tiny-imagenet.herokuapp.com/>, Accessed: 2023. A subset of the ImageNet dataset.
- Acar, D. A. E., Zhao, Y., Matas, R., Mattina, M., Whatmough, P., and Saligrama, V. Federated learning based on dynamic regularization. In *International Conference on Learning Representations*, 2020.
- Adilova, L., Fischer, A., and Jaggi, M. Layerwise linear mode connectivity. *arXiv preprint arXiv:2307.06966*, 2023.
- Ainsworth, S., Hayase, J., and Srinivasa, S. Git re-basin: Merging models modulo permutation symmetries. In *The Eleventh International Conference on Learning Representations*, 2022.
- Akyürek, A. F., Akyürek, E., Wijaya, D., and Andreas, J. Subspace regularizers for few-shot class incremental learning. In *International Conference on Learning Representations*, 2021.
- Chaudhry, A., Khan, N., Dokania, P., and Torr, P. Continual learning in low-rank orthogonal subspaces. *Advances in Neural Information Processing Systems*, 33:9900–9911, 2020.
- Chen, H.-Y. and Chao, W.-L. On bridging generic and personalized federated learning for image classification. In *International Conference on Learning Representations*, 2022.
- Dai, Y., Chen, Z., Li, J., Heinecke, S., Sun, L., and Xu, R. Tackling data heterogeneity in federated learning with class prototypes. 2023.
- Deng, J., Dong, W., Socher, R., Li, L.-J., Li, K., and Fei-Fei, L. Imagenet: A large-scale hierarchical image database. *2009 IEEE conference on computer vision and pattern recognition*, pp. 248–255, 2009.
- Don-Yehiya, S., Venezian, E., Raffel, C., Slonim, N., and Choshen, L. Cold fusion: Collaborative descent for distributed multitask finetuning. In Rogers, A., Boyd-Graber, J. L., and Okazaki, N. (eds.), *Proceedings of the 61st Annual Meeting of the Association for Computational Linguistics (Volume 1: Long Papers)*, *ACL 2023, Toronto, Canada, July 9-14, 2023*, pp. 788–806. Association for Computational Linguistics, 2023. doi: 10.18653/V1/2023.ACL-LONG.46. URL <https://doi.org/10.18653/v1/2023.acl-long.46>.
- Dosovitskiy, A., Beyer, L., Kolesnikov, A., Weissenborn, D., Zhai, X., Unterthiner, T., Dehghani, M., Minderer, M., Heigold, G., Gelly, S., et al. An image is worth 16x16 words: Transformers for image recognition at scale. In *International Conference on Learning Representations*, 2021.
- Draxler, F., Veschgini, K., Salmhofer, M., and Hamprecht, F. Essentially no barriers in neural network energy landscape. In *International conference on machine learning*, pp. 1309–1318. PMLR, 2018.
- Du, J., Yan, H., Feng, J., Zhou, J. T., Zhen, L., Goh, R. S. M., and Tan, V. Y. Efficient sharpness-aware minimization for improved training of neural networks. *arXiv preprint arXiv:2110.03141*, 2021.
- Entezari, R., Sedghi, H., Saukh, O., and Neyshabur, B. The role of permutation invariance in linear mode connectivity of neural networks. In *International Conference on Learning Representations*, 2022.
- Foret, P., Kleiner, A., Mobahi, H., and Neyshabur, B. Sharpness-aware minimization for efficiently improving generalization. *arXiv preprint arXiv:2010.01412*, 2020.
- Fort, S. and Jastrzebski, S. Large scale structure of neural network loss landscapes. *Advances in Neural Information Processing Systems*, 32, 2019.
- Frankle, J., Dziugaite, G. K., Roy, D., and Carbin, M. Linear mode connectivity and the lottery ticket hypothesis. In *International Conference on Machine Learning*, pp. 3259–3269. PMLR, 2020.
- Garipov, T., Izmailov, P., Podoprikin, D., Vetrov, D. P., and Wilson, A. G. Loss surfaces, mode connectivity, and fast ensembling of dnns. *Advances in neural information processing systems*, 31, 2018.
- Graves, A. and Graves, A. Long short-term memory. *Supervised sequence labelling with recurrent neural networks*, pp. 37–45, 2012.
- Gressmann, F., Eaton-Rosen, Z., and Luschi, C. Improving neural network training in low dimensional random bases. *Advances in Neural Information Processing Systems*, 33: 12140–12150, 2020.
- Hahn, S.-J., Jeong, M., and Lee, J. Connecting low-loss subspace for personalized federated learning. In *Proceedings of the 28th ACM SIGKDD Conference on Knowledge Discovery and Data Mining*, pp. 505–515, 2022.

- He, K., Zhang, X., Ren, S., and Sun, J. Deep residual learning for image recognition. In *Proceedings of the IEEE conference on computer vision and pattern recognition*, pp. 770–778, 2016.
- Hecht-Nielsen, R. On the algebraic structure of feedforward network weight spaces. In *Advanced Neural Computers*, pp. 129–135. Elsevier, 1990.
- Hu, E. J., Wallis, P., Allen-Zhu, Z., Li, Y., Wang, S., Wang, L., Chen, W., et al. Lora: Low-rank adaptation of large language models. In *International Conference on Learning Representations*, 2021.
- Isik, B., Pase, F., Gunduz, D., Weissman, T., and Michele, Z. Sparse random networks for communication-efficient federated learning. In *The Eleventh International Conference on Learning Representations*, 2022.
- Izmailov, P., Wilson, A., Podoprikin, D., Vetrov, D., and Garipov, T. Averaging weights leads to wider optima and better generalization. In *34th Conference on Uncertainty in Artificial Intelligence 2018, UAI 2018*, pp. 876–885, 2018.
- Jastrzębski, S., Kenton, Z., Ballas, N., Fischer, A., Bengio, Y., and Storkey, A. On the relation between the sharpest directions of dnn loss and the sgd step length. *arXiv preprint arXiv:1807.05031*, 2018.
- Krizhevsky, A. et al. Learning multiple layers of features from tiny images. *Citeseer*, 2009.
- Kwon, J., Kim, J., Park, H., and Choi, I. K. Asam: Adaptive sharpness-aware minimization for scale-invariant learning of deep neural networks. In *International Conference on Machine Learning*, pp. 5905–5914. PMLR, 2021.
- LeCun, Y. and Cortes, C. MNIST handwritten digit database. *arxiv*, 2010. URL <http://yann.lecun.com/exdb/mnist/>.
- LeCun, Y., Bottou, L., Bengio, Y., and Haffner, P. Gradient-based learning applied to document recognition. *Proceedings of the IEEE*, 86(11):2278–2324, 1998.
- Lee, S., Sahu, A. K., He, C., and Avestimehr, S. Partial model averaging in federated learning: Performance guarantees and benefits. *Neurocomputing*, 556:126647, 2023.
- Li, A., Sun, J., Zeng, X., Zhang, M., Li, H., and Chen, Y. Fedmask: Joint computation and communication-efficient personalized federated learning via heterogeneous masking. In *Proceedings of the 19th ACM Conference on Embedded Networked Sensor Systems*, pp. 42–55, 2021.
- Li, C., Farkhoor, H., Liu, R., and Yosinski, J. Measuring the intrinsic dimension of objective landscapes. In *International Conference on Learning Representations*, 2018a.
- Li, H., Xu, Z., Taylor, G., Studer, C., and Goldstein, T. Visualizing the loss landscape of neural nets. *Advances in neural information processing systems*, 31, 2018b.
- Li, T., Sahu, A. K., Zaheer, M., Sanjabi, M., Talwalkar, A., and Smith, V. Federated optimization in heterogeneous networks. *Proceedings of Machine Learning and Systems*, 2:429–450, 2020a.
- Li, X., JIANG, M., Zhang, X., Kamp, M., and Dou, Q. Fedbn: Federated learning on non-iid features via local batch normalization. In *International Conference on Learning Representations*, 2020b.
- Li, X.-C., Xu, Y.-C., Song, S., Li, B., Li, Y., Shao, Y., and Zhan, D.-C. Federated learning with position-aware neurons. In *Proceedings of the IEEE/CVF Conference on Computer Vision and Pattern Recognition*, pp. 10082–10091, 2022.
- Li, Z., Lin, T., Shang, X., and Wu, C. Revisiting weighted aggregation in federated learning with neural networks. In *Proceedings of the 40th International Conference on Machine Learning*, volume 202 of *Proceedings of Machine Learning Research*, pp. 19767–19788. PMLR, 23–29 Jul 2023a.
- Li, Z., Shang, X., He, R., Lin, T., and Wu, C. No fear of classifier biases: Neural collapse inspired federated learning with synthetic and fixed classifier. In *Proceedings of the IEEE/CVF International Conference on Computer Vision (ICCV)*, pp. 5319–5329, October 2023b.
- Lin, T., Kong, L., Stich, S. U., and Jaggi, M. Ensemble distillation for robust model fusion in federated learning. *Advances in Neural Information Processing Systems*, 33: 2351–2363, 2020.
- Lin, Y., Han, S., Mao, H., Wang, Y., and Dally, B. Deep gradient compression: Reducing the communication bandwidth for distributed training. In *International Conference on Learning Representations*, 2018.
- Liu, C., Lou, C., Wang, R., Xi, A. Y., Shen, L., and Yan, J. Deep neural network fusion via graph matching with applications to model ensemble and federated learning. In *International Conference on Machine Learning*, pp. 13857–13869. PMLR, 2022a.
- Liu, Z., Michaud, E. J., and Tegmark, M. Omnigrok: Grokking beyond algorithmic data. In *The Eleventh International Conference on Learning Representations*, 2022b.

- Lubana, E. S., Bigelow, E. J., Dick, R. P., Krueger, D., and Tanaka, H. Mechanistic mode connectivity. In *International Conference on Machine Learning*, pp. 22965–23004. PMLR, 2023.
- Maas, A., Daly, R. E., Pham, P. T., Huang, D., Ng, A. Y., and Potts, C. Learning word vectors for sentiment analysis. In *Proceedings of the 49th annual meeting of the association for computational linguistics: Human language technologies*, pp. 142–150, 2011.
- McMahan, B., Moore, E., Ramage, D., Hampson, S., and y Arcas, B. A. Communication-efficient learning of deep networks from decentralized data. In *Artificial intelligence and statistics*, pp. 1273–1282. PMLR, 2017.
- Neyshabur, B., Bhojanapalli, S., McAllester, D., and Srebro, N. Exploring generalization in deep learning. *Advances in neural information processing systems*, 30, 2017.
- Niu, Y., Prakash, S., Kundu, S., Lee, S., and Avestimehr, S. Federated learning of large models at the edge via principal sub-model training. In *Workshop on Federated Learning: Recent Advances and New Challenges (in Conjunction with NeurIPS 2022)*, 2022.
- Peña, F. A. G., Medeiros, H. R., Dubail, T., Aminbeidokhti, M., Granger, E., and Pedersoli, M. Re-basin via implicit sinkhorn differentiation. In *Proceedings of the IEEE/CVF Conference on Computer Vision and Pattern Recognition*, pp. 20237–20246, 2023.
- Radford, A., Narasimhan, K., Salimans, T., and Sutskever, I. Improving language understanding by generative pre-training. 2018.
- Radford, A., Kim, J. W., Hallacy, C., Ramesh, A., Goh, G., Agarwal, S., Sastry, G., Askell, A., Mishkin, P., Clark, J., Krueger, G., and Sutskever, I. Learning transferable visual models from natural language supervision. In Meila, M. and Zhang, T. (eds.), *Proceedings of the 38th International Conference on Machine Learning*, volume 139 of *Proceedings of Machine Learning Research*, pp. 8748–8763. PMLR, 18–24 Jul 2021. URL <https://proceedings.mlr.press/v139/radford21a.html>.
- Safran, I. and Shamir, O. Spurious local minima are common in two-layer relu neural networks. In *International conference on machine learning*, pp. 4433–4441. PMLR, 2018.
- Simsek, B., Ged, F., Jacot, A., Spadaro, F., Hongler, C., Gerstner, W., and Brea, J. Geometry of the loss landscape in overparameterized neural networks: Symmetries and invariances. In *International Conference on Machine Learning*, pp. 9722–9732. PMLR, 2021.
- Singh, S. P. and Jaggi, M. Model fusion via optimal transport. *Advances in Neural Information Processing Systems*, 33:22045–22055, 2020.
- Tatro, N., Chen, P.-Y., Das, P., Melnyk, I., Sattigeri, P., and Lai, R. Optimizing mode connectivity via neuron alignment. *Advances in Neural Information Processing Systems*, 33:15300–15311, 2020.
- Vlaar, T. J. and Frankle, J. What can linear interpolation of neural network loss landscapes tell us? In *International Conference on Machine Learning*, pp. 22325–22341. PMLR, 2022.
- Vogels, T., Karimireddy, S. P., and Jaggi, M. Powersgd: Practical low-rank gradient compression for distributed optimization. *Advances in Neural Information Processing Systems*, 32, 2019.
- von Oswald, J., Henning, C., Grewe, B. F., and Sacramento, J. Continual learning with hypernetworks. In *International Conference on Learning Representations*, 2019.
- Wang, A., Singh, A., Michael, J., Hill, F., Levy, O., and Bowman, S. R. Glue: A multi-task benchmark and analysis platform for natural language understanding. In *Proceedings of the International Conference on Learning Representations (ICLR)*, 2019. URL <https://openreview.net/forum?id=rJ4km2R5t7>.
- Wang, H., Yurochkin, M., Sun, Y., Papailiopoulos, D., and Khazaeni, Y. Federated learning with matched averaging. In *International Conference on Learning Representations*, 2020a.
- Wang, H., Yurochkin, M., Sun, Y., Papailiopoulos, D., and Khazaeni, Y. Federated learning with matched averaging. *arXiv preprint arXiv:2002.06440*, 2020b.
- Wortsman, M., Ilharco, G., Gadre, S. Y., Roelofs, R., Gontijo-Lopes, R., Morcos, A. S., Namkoong, H., Farhadi, A., Carmon, Y., Kornblith, S., et al. Model soups: averaging weights of multiple fine-tuned models improves accuracy without increasing inference time. In *International Conference on Machine Learning*, pp. 23965–23998. PMLR, 2022.
- Xiao, H., Rasul, K., and Vollgraf, R. Fashion-mnist: a novel image dataset for benchmarking machine learning algorithms. *arXiv preprint arXiv:1708.07747*, 2017.
- Yang, T.-J., Guliani, D., Beaufays, F., and Motta, G. Partial variable training for efficient on-device federated learning. In *ICASSP 2022-2022 IEEE International Conference on Acoustics, Speech and Signal Processing (ICASSP)*, pp. 4348–4352. IEEE, 2022.

- Yao, Z., Gholami, A., Keutzer, K., and Mahoney, M. W. Py-hessian: Neural networks through the lens of the hessian. In *2020 IEEE international conference on big data (Big data)*, pp. 581–590. IEEE, 2020.
- Yurochkin, M., Agarwal, M., Ghosh, S., Greenewald, K., Hoang, N., and Khazaeni, Y. Bayesian nonparametric federated learning of neural networks. In *International conference on machine learning*, pp. 7252–7261. PMLR, 2019.
- Zhang, C., Bengio, S., Hardt, M., Recht, B., and Vinyals, O. Understanding deep learning (still) requires rethinking generalization. *Communications of the ACM*, 64(3):107–115, 2021.
- Zhao, P., Chen, P.-Y., Das, P., Ramamurthy, K. N., and Lin, X. Bridging mode connectivity in loss landscapes and adversarial robustness. In *International Conference on Learning Representations (ICLR 2020)*, 2020.

Appendix

In this appendix, we provide the details omitted in the main paper and more analyses and discussions.

- **Appendix A:** details of experimental setups (cf. [section 3](#) and [section 4](#) of the main paper).
- **Appendix B:** detailed proof of [Theorem 3.2](#) (cf. [section 3](#) of the main paper).
- **Appendix C:** additional results and analyses (cf. [section 3](#) and [section 4](#) of the main paper).
- **Appendix D:** preliminary of federated learning (cf. [section 2](#) and [section 4](#)).
- **Appendix E:** more discussions about the related works (cf. [section 2](#) of the main paper).

A. Implementation Details

In this section, we provide the additional implementation details in [section 3](#) and [section 4](#).

A.1. Datasets

MNIST ([LeCun & Cortes, 2010](#)) comprises a collection of 70,000 handwritten digits (0-9), divided into 60,000 training images and 10,000 testing images. Each image is grayscale and has a dimension of 28x28 pixels. **CIFAR-10** ([Krizhevsky et al., 2009](#)) consists of 60,000 32x32 color images, evenly distributed across 10 different classes or labels, such as airplanes, automobiles, birds, cats, etc., each represented by 6,000 images. The dataset is split into 50,000 training images and 10,000 test images. **The polynomial approximation dataset** ([Peña et al., 2023](#); [von Oswald et al., 2019](#)) is the synthetic dataset of the second and third polynomial functions: $y = 2x^2 - 1$, $y = (x - 3)^3$. The input of the second polynomial function is uniformly generated from $x \in [-1.0, 1.0]$ with 100 data points, and the input of the third polynomial function is uniformly generated from $x \in [2.0, 4.0]$ with 100 data points. Each y label in both the second and the third polynomial datasets is added by a random Gaussian noise with zero mean and 0.05 std. The **IMDb** (Internet Movie Database) ([Maas et al., 2011](#)) dataset is a popular dataset used in Natural Language Processing (NLP) and sentiment analysis tasks. It consists of 50,000 movie reviews, evenly split into 25,000 reviews for training and 25,000 reviews for testing, each labeled as either positive or negative. **FashionMNIST** ([Xiao et al., 2017](#)) is a dataset designed as a more advanced replacement for the MNIST dataset, suitable for benchmarking machine learning models. It consists of 70,000 images divided into 60,000 training samples and 10,000 test samples. Each image is a 28x28 grayscale representation of fashion items from 10 different classes, including shirts, trousers, sneakers, etc. The **CIFAR-100** dataset ([Krizhevsky et al., 2009](#)) is similar to the CIFAR-10 dataset but more challenging as it contains 100 different classes grouped into 20 superclasses. It contains 60,000 32x32 color images, with 600 images per class, divided into 50,000 training images and 10,000 test images. This dataset is primarily used for developing and evaluating more sophisticated image classification models.

A.2. Models

CNN and MLP. The simple CNN for CIFAR-10 and CIFAR-100 is a convolution neural network model with ReLU activations, which consists of 3 convolutional layers followed by 2 fully connected layers. The first convolutional layer is of size (3, 32, 3), followed by a max pooling layer of size (2, 2). The second and third convolutional layers are of sizes (32, 64, 3) and (64, 64, 3), respectively. The last two connected layers are of sizes (64*4*4, 64) and (64, num_classes), respectively. The MLP model MLP_h2_w200 stands for an MLP with 2 hidden layers and a width of 200 in each layer. We vary h and w in [Figure 3](#) to see the barriers in linear mode connectivity. We use MLP_h2_w200 for the MLP model in [Table 5](#).

ResNets. We followed the model architectures used in ([Li et al., 2018b](#)). The number of the model names means the number of layers of the models. Naturally, the larger number indicates a deeper network. For WRN56 in [Figure 4](#), it is an abbreviation of Wide-ResNet56-4, where "4" refers to four times as many filters per layer. The ResNets used in [Table 5](#) are ResNet20 for CIFAR-10 and CIFAR-100. It is notable that since the batch normalization layers will have abnormal effects on model fusion ([Li et al., 2020b](#); [Lin et al., 2020](#)), following ([Adilova et al., 2023](#)), we remove all the batch normalization layers from the ResNets.

A.3. Randomness

In all experiments, we implement the experiments three times with different random seeds and report the averaged results with standard deviations.

For the experiments in linear mode connectivity, within a set of experiments, we generate an initial model according to the random seed a and conduct training, then, we set the random seed as $a + 1$ and load the initial model from random seed a and conduct another independent training; afterward, the linear connectivity of the two models are tested.

For the experiments in federated learning. Given a random seed, we set torch, numpy, and random functions as the same random seed to make the data partitions and other settings identical. To make sure all algorithms have the same initial model, we save an initial model for each architecture and load the saved initial model at the beginning of one experiment. Also, for the experiments with partial participation, the participating clients in each round are vital in determining the model performance, and to guarantee fairness, we save the sequences of participating clients in each round and load the sequences in all experiments. This will make sure that, given a random seed and participation ratio, every algorithm will have the same sampled clients in each round.

A.4. Evaluation

Linear mode connectivity. We validate all the accuracy and loss barriers on the test datasets to indicate the model generalization.

Federated learning. We evaluate the global model performance on the test dataset of each dataset. The test dataset is mostly class-balanced and can reflect the global learning objective of a federated learning system. Therefore, the performance of the model on the test set can indicate the generalization performance of global models (Li et al., 2023a; Lin et al., 2020). In each experiment, we run 100 rounds and take the average test accuracy of the last 5 rounds as the final test accuracy.

A.5. Hyperparameter

Linear mode connectivity. For CIFAR-10 and MNIST, We set a fixed learning rate of 0.1 and use the SGD optimizer with a weight decay of $5e-4$ and momentum of 0.9; the number of learning epochs is 10. For the Polynomial datasets, the learning rate is 0.05 for 100 epochs. For the IMDB dataset, the learning rate is 0.0005 for 20 epochs.

Federated learning. We set the initial learning rates as 0.08 in CIFAR-10 and FashionMNIST and set it as 0.05 in CIFAR-100. Following (Li et al., 2023a; Chen & Chao, 2022), we set a decaying learning rate scheduler in all experiments; that is, in each round, the local learning rate is $0.99 \times$ (the learning rate of the last round). We set the weight decay factor as $5e-4$. We set SGD optimizer as the clients’ local solver and set momentum as 0.9.

For the server-side optimizer FedDF, the server-side learning rate is 0.01 and the number of epochs is 20. We set $\mu = 0.001$ for FedProx.

A.6. Pseudo-codes

We present the pseudo-codes of the federated learning methods FedPFN and FedPNU in [Algorithm 1](#) and [Algorithm 2](#).

Algorithm 1 FedPFN: Federated Learning with Partially Fixed Neurons

Input: clients $\{1, \dots, n\}$, mask ratio ρ , comm. round T , local epoch E , initial global model \mathbf{w}_g^1 ;

Output: final global model \mathbf{w}_g^T ;

- 1: **for** each round $t = 1, \dots, T$ **do**
 - 2: # Client updates
 - 3: **for** each client $i, i \in [n]$ **in parallel do**
 - 4: Receive global model \mathbf{w}_g^t and neuron mask \mathbf{m}^t ;
 - 5: Set local model $\mathbf{w}_i^t \leftarrow \mathbf{w}_g^t$;
 - 6: Compute E epochs of client local training by [Equation 9](#):
 - 7: $\mathbf{w}_i^t \leftarrow \mathbf{w}_i^t - \eta_l(\mathbf{m}^t \odot \mathbf{g}_i(\mathbf{w}_i^t))$;
 - 8: **end for**
 - 9: # Server updates
 - 10: The server samples m clients and receive their models $\{\mathbf{w}_i^t\}_{i=1}^m$;
 - 11: Obtain the global model by FedAvg:
 - 12: $\mathbf{w}_g^{t+1} \leftarrow \sum_{i=1}^m \lambda_i \mathbf{w}_i^t$, where λ_i is the aggregation weight of client i ;
 - 13: Randomly generate the new neuron mask \mathbf{m}^{t+1} according to the ratio ρ .
 - 14: **end for**
 - 15: Obtain the final global model \mathbf{w}_g^T .
-

Algorithm 2 FedPNU: Federated Learning with Progressive Neuron Updating
Input: clients $\{1, \dots, n\}$, mask ratio ρ , comm. round T , local epoch E , initial global model \mathbf{w}_g^1 ;

Output: final global model \mathbf{w}_g^T ;

```

1: for each round  $t = 1, \dots, T$  do
2:   # Client updates
3:   for each client  $i, i \in [n]$  in parallel do
4:     Receive global model  $\mathbf{w}_g^t$  and neuron mask  $\mathbf{m}^t$ ;
5:     Set local model  $\mathbf{w}_i^t \leftarrow \mathbf{w}_g^t$  and compute the reverse mask  $\hat{\mathbf{m}}^t$  of  $\mathbf{m}^t$ ;
6:     Compute  $\text{int}(\frac{E}{2})$  epochs of client local training by Equation 9:
7:        $\mathbf{w}_i^t \leftarrow \mathbf{w}_i^t - \eta_l(\mathbf{m}^t \odot \mathbf{g}_i(\mathbf{w}_i^t))$ ;
8:     Compute  $E - \text{int}(\frac{E}{2})$  epochs of client local training by Equation 9:
9:        $\mathbf{w}_i^t \leftarrow \mathbf{w}_i^t - \eta_l(\hat{\mathbf{m}}^t \odot \mathbf{g}_i(\mathbf{w}_i^t))$ ;
10:   end for
11:   # Server updates
12:   The server samples  $m$  clients and receive their models  $\{\mathbf{w}_i^t\}_{i=1}^m$ ;
13:   Obtain the global model by FedAvg:
14:    $\mathbf{w}_g^{t+1} \leftarrow \sum_{i=1}^m \lambda_i \mathbf{w}_i^t$ , where  $\lambda_i$  is the aggregation weight of client  $i$ ;
15:   Randomly generate the new neuron mask  $\mathbf{m}^{t+1}$  according to the ratio  $\rho$ .
16: end for
17: Obtain the final global model  $\mathbf{w}_g^T$ .
    
```

B. Proof of Theorem 3.2

We first recap the Theorem 3.2 for convenience and provide the proof.

Theorem B.1. We define a two-layer neural network with ReLU activation, and the function is $f_{\mathbf{v}, \mathbf{U}}(\mathbf{x}) = \mathbf{v}^\top \sigma(\mathbf{U}\mathbf{x})$ where $\sigma(\cdot)$ is the ReLU activation function. $\mathbf{v} \in \mathbb{R}^h$ and $\mathbf{U} \in \mathbb{R}^{h \times d}$ are parameters³ and $\mathbf{x} \in \mathbb{R}^d$ is the input which is taken from $\mathbb{X} = \{\mathbf{x} \in \mathbb{R}^d \mid \|\mathbf{x}\|_2 < b\}$ uniformly. Consider two different networks parameterized with $\{\mathbf{U}, \mathbf{v}\}$ and $\{\mathbf{U}', \mathbf{v}'\}$ respectively, and for arbitrarily chosen masks $\mathbf{M}_v \in \{0, 1\}^h$ and $\mathbf{M}_U \in \{0, 1\}^{h \times d}$, each element of \mathbf{U} and \mathbf{U}' , \mathbf{v} and \mathbf{v}' is i.i.d. sampled from a sub-Gaussian distribution $\text{sub-G}(0, \sigma_v^2)$ and $\text{sub-G}(0, \sigma_U^2)$ respectively with setting $v_i = v'_i$ when $M_{v,i} = 0$ and $U_{i,j} = U'_{i,j}$ when $M_{U,ij} = 0$. We consider the linear mode connectivity of the two networks and define the difference function between interpolated network and original networks as $z_{\mathbf{x}}(\alpha) = (\alpha\mathbf{v} + (1-\alpha)\mathbf{v}')^\top \sigma((\alpha\mathbf{U} + (1-\alpha)\mathbf{U}')\mathbf{x}) - \alpha\mathbf{v}^\top \sigma(\mathbf{U}\mathbf{x}) - (1-\alpha)\mathbf{v}'^\top \sigma(\mathbf{U}'\mathbf{x})$, $\alpha \in [0, 1]$. The function over all inputs is defined as $z(\alpha) = \frac{1}{|\mathbb{X}|} \int_{\mathbb{X}} z_{\mathbf{x}}(\alpha) d\mathbf{x}$. We use $|z(\alpha)|$, $\left| \frac{dz(\alpha)}{d\alpha} \right|$ and $\left| \frac{d^2z(\alpha)}{d\alpha^2} \right|$ to depict the linear mode connectivity, showing the output changes along the α path. With probability $1 - \delta$, it has,

$$|z(\alpha)| \leq \sqrt{2}b\sigma_v\sigma_U \log(8h/\delta) \sqrt{h} \sqrt{1 - \rho_U}, \quad (10)$$

$$\left| \frac{dz(\alpha)}{d\alpha} \right| \leq 4\sqrt{2}b\sigma_v\sigma_U \log(24h/\delta) \sqrt{h} (\sqrt{1 - \rho_v} + \sqrt{1 - \rho_U}), \quad (11)$$

$$\left| \frac{d^2z(\alpha)}{d\alpha^2} \right| \leq 8b\sigma_v\sigma_U \log(4h/\delta) \sqrt{h} \sqrt{1 - \max\{\rho_U, \rho_v\}}, \quad (12)$$

where ρ_v and ρ_U refer to the mask ratios (the proportion of zeros in the mask) of masks \mathbf{M}_v and \mathbf{M}_U respectively.

Proof: Let's first define $g_\alpha(\mathbf{x}) = (\alpha\mathbf{U} + (1-\alpha)\mathbf{U}')\mathbf{x}$. Then we can express $z_{\mathbf{x}}(\alpha)$ as:

$$z_{\mathbf{x}}(\alpha) = (\alpha\mathbf{v} + (1-\alpha)\mathbf{v}')^\top \sigma(g_\alpha(\mathbf{x})) - \alpha\mathbf{v}^\top \sigma(\mathbf{U}\mathbf{x}) - (1-\alpha)\mathbf{v}'^\top \sigma(\mathbf{U}'\mathbf{x}). \quad (13)$$

The first derivative of $z_{\mathbf{x}}(\alpha)$ with respect to α will be:

$$\frac{dz_{\mathbf{x}}(\alpha)}{d\alpha} = (\mathbf{v} - \mathbf{v}')^\top \sigma(g_\alpha(\mathbf{x})) + (\alpha\mathbf{v} + (1-\alpha)\mathbf{v}')^\top \sigma'(g_\alpha(\mathbf{x})) - \mathbf{v}^\top \sigma(\mathbf{U}\mathbf{x}) + \mathbf{v}'^\top \sigma(\mathbf{U}'\mathbf{x}). \quad (14)$$

³For simplicity and without loss of generality, we omit the bias terms.

The second derivative with respect to α will be:

$$\frac{d^2 z_{\mathbf{x}}(\alpha)}{d\alpha^2} = 2(\mathbf{v} - \mathbf{v}')^\top \sigma'(g_\alpha(\mathbf{x})) + (\alpha\mathbf{v} + (1 - \alpha)\mathbf{v}')^\top \sigma''(g_\alpha(\mathbf{x})). \quad (15)$$

We also assume that the number of hidden neurons h is sufficiently large for the convenience of analysis as (Entezari et al., 2022) and we use $\#\{\mathbf{M}_{\mathbf{U}} = i\}$ and $\#\{\mathbf{M}_{\mathbf{v}} = i\}$ denote the number of i in $\mathbf{M}_{\mathbf{U}}$ and $\mathbf{M}_{\mathbf{v}}$ respectively, $i = 1, 2$. In the following proof, we will make use of Hoeffding's inequality for sub-Gaussian distributions. Here, we state it for reference: Let X_1, \dots, X_n be n independent random variables such that $X_i \sim \text{sub-G}(0, \sigma^2)$. Then for any $\mathbf{a} = (a_1, \dots, a_n) \in \mathbb{R}^n$, we have

$$\mathbb{P} \left[\left| \sum_{i=1}^n a_i X_i \right| > t \right] \leq 2 \exp \left(-\frac{t^2}{2\sigma^2 \|\mathbf{a}\|_2^2} \right).$$

1) For the 0-order difference equation, we have

$$|z_{\mathbf{x}}(\alpha)| = \left| \alpha \mathbf{v}^\top [\sigma(g_\alpha(\mathbf{x})) - \sigma(\mathbf{U}\mathbf{x})] + (1 - \alpha) \mathbf{v}'^\top [\sigma(g_\alpha(\mathbf{x})) - \sigma(\mathbf{U}'\mathbf{x})] \right| \quad (16)$$

$$\leq \alpha \left| \mathbf{v}^\top [(\sigma(g_\alpha(\mathbf{x})) - \sigma(\mathbf{U}\mathbf{x}))] \right| + (1 - \alpha) \left| \mathbf{v}'^\top [\sigma(g_\alpha(\mathbf{x})) - \sigma(\mathbf{U}'\mathbf{x})] \right|. \quad (17)$$

Then we bound the first term and the second term is bounded similarly due to symmetry. For the **concentration upper bound** of the first term of Equation 17, we use the Hoeffding's inequality for elements of \mathbf{v} , with probability $1 - \frac{\delta}{k}$

$$\alpha \left| \mathbf{v}^\top [(\sigma(g_\alpha(\mathbf{x})) - \sigma(\mathbf{U}\mathbf{x}))] \right| \leq \alpha \sigma_v \sqrt{2 \log(2k/\delta)} \|\sigma(g_\alpha(\mathbf{x})) - \sigma(\mathbf{M}\mathbf{x})\|_2 \quad (18)$$

$$\leq \alpha \sigma_v \sqrt{2 \log(2k/\delta)} \|\mathbf{g}_\alpha(\mathbf{x}) - \mathbf{M}\mathbf{x}\|_2 \quad (19)$$

$$= \alpha(1 - \alpha) \sigma_v \sqrt{2 \log(2k/\delta)} \|(\mathbf{U}' - \mathbf{U})\mathbf{x}\|_2. \quad (20)$$

Equation 19 is due to the fact that the ReLU activation function satisfies the Lipschitz continuous condition with constant 1. For the item $\|(\mathbf{U} - \mathbf{U}')\mathbf{x}\|_2$, notice that $U_{ij} = U'_{ij}$ when $M_{U,ij} = 0$, and then take a union bound, with probability $1 - \frac{\delta}{k}$, we have

$$\|(\mathbf{U} - \mathbf{U}')\mathbf{x}\|_2 \leq \sqrt{\sum_{i=1}^h |[\mathbf{M}_{\mathbf{U},i} \odot (\mathbf{U}_{i,:} - \mathbf{U}'_{i,:})\mathbf{x}]|^2} \quad (21)$$

$$= \sqrt{\sum_{i=1}^h |(\mathbf{U}_{i,:} - \mathbf{U}'_{i,:})(\mathbf{M}_{\mathbf{U},i} \odot \mathbf{x})|^2} \quad (22)$$

$$\leq \sigma_{\mathbf{U}} \sqrt{\sum_{i=1}^h \|\mathbf{M}_{\mathbf{U},i} \odot \mathbf{x}\|_2^2 \sqrt{4 \log(2hk/\delta)}}. \quad (23)$$

Then take a union bound choosing $k = 4$ (because the union bound is taken for 4 equations, Equation 20 and Equation 23 for the first and the second terms in Equation 17 respectively. Subsequent values of k are determined with a similar method.), with probability $1 - \delta$ we have

$$|z_{\mathbf{x}}(\alpha)| < 4\sqrt{2}\alpha(1 - \alpha)\sigma_v\sigma_{\mathbf{U}} \log(8h/\delta) \sqrt{\sum_{i=1}^h \|\mathbf{M}_{\mathbf{U},i} \odot \mathbf{x}\|_2^2}. \quad (24)$$

Then integrate it on the region \mathbb{X} . With probability $1 - \delta$, we have

$$|z(\alpha)| \leq 4\sqrt{2}\alpha(1 - \alpha)\sigma_v\sigma_{\mathbf{U}} \log(8h/\delta) b \sqrt{\frac{d}{d+2}} \sqrt{h - \frac{\#\{\mathbf{M}_{\mathbf{v}} = 0\}}{d}} \quad (25)$$

$$\leq \sqrt{2}\sigma_v\sigma_{\mathbf{U}} \log(8h/\delta) b \sqrt{h - \frac{\#\{\mathbf{M}_{\mathbf{v}} = 0\}}{d}} \quad (26)$$

$$= \sqrt{2}\sigma_v\sigma_{\mathbf{U}} \log(8h/\delta) b \sqrt{h} \sqrt{1 - \rho_{\mathbf{U}}}. \quad (27)$$

Equation 25 is due to fact that the integration $\frac{1}{|\mathbb{X}|} \int_{\mathbb{X}} \sqrt{\sum_{i=1}^h \|\mathbf{M}_{\mathbf{U},i} \odot \mathbf{x}\|_2^2} d\mathbf{x}$ satisfies

$$\frac{1}{|\mathbb{X}|} \int_{\mathbb{X}} \sqrt{\sum_{i=1}^h \|\mathbf{M}_{\mathbf{U},i} \odot \mathbf{x}\|_2^2} d\mathbf{x} \leq \sqrt{\left(\frac{1}{|\mathbb{X}|} \int_{\mathbb{X}} \sum_{i=1}^h \|\mathbf{M}_{\mathbf{U},i} \odot \mathbf{x}\|_2^2 d\mathbf{x}\right) \left(\frac{1}{|\mathbb{X}|} \int_{\mathbb{X}} d\mathbf{x}\right)} \quad (28)$$

$$= \sqrt{\frac{1}{|\mathbb{X}|} \int_{\mathbb{X}} \#\{\mathbf{M}_{\mathbf{U}} = 1\} x_i^2 d\mathbf{x}} \quad (29)$$

$$= \sqrt{\frac{\#\{\mathbf{M}_{\mathbf{U}} = 1\}}{d} \frac{1}{|\mathbb{X}|} \int_{\mathbb{X}} \|\mathbf{x}\|_2^2 d\mathbf{x}} \quad (30)$$

$$= \sqrt{\left(h - \frac{\#\{\mathbf{M}_{\mathbf{U}} = 0\}}{d}\right) \frac{db^2}{d+2}}, \quad (31)$$

where Equation 28 is due to Cauchy-Schwarz inequality of integration, Equation 29 and Equation 30 is due to the symmetry of different components of \mathbf{x} and Equation 31 is due to the integration $\frac{1}{|\mathbb{X}|} \int_{\mathbb{X}} \|\mathbf{x}\|_2^k d\mathbf{x} = \frac{db^k}{d+k}$, $k \in \mathbb{Z}$.

2) For the first derivative, we have

$$\left| \frac{dz_{\mathbf{x}}(\alpha)}{d\alpha} \right| \leq |(\mathbf{v} - \mathbf{v}')^\top \sigma(g_{\alpha}(\mathbf{x}))| + |(\alpha \mathbf{v} + (1 - \alpha) \mathbf{v}')^\top \sigma'(g_{\alpha}(\mathbf{x}))| + |v^\top \sigma(\mathbf{U}\mathbf{x}) - v'^\top \sigma(\mathbf{U}'\mathbf{x})|. \quad (32)$$

i) For the **concentration upper bound** of the first term of Equation 32, we use the Hoeffding's inequality for elements of $\mathbf{v} - \mathbf{v}'$ and notice that $v_i - v'_i = 0$ when $M_{\mathbf{v},i} = 0$, with probability $1 - \frac{\delta}{k}$

$$|(\mathbf{v} - \mathbf{v}')^\top \sigma(g_{\alpha}(\mathbf{x}))| \leq \sigma_{\mathbf{v}} \sqrt{4 \log(2k/\delta)} \|\mathbf{M}_{\mathbf{v}} \odot \sigma(g_{\alpha}(\mathbf{x}))\|_2 \quad (33)$$

$$\leq \sigma_{\mathbf{v}} \sqrt{4 \log(2k/\delta)} \|\mathbf{M}_{\mathbf{v}} \odot g_{\alpha}(\mathbf{x})\|_2 \quad (34)$$

$$\leq \sigma_{\mathbf{v}} \sqrt{4 \log(2k/\delta)} (\alpha \|\mathbf{M}_{\mathbf{v}} \odot \mathbf{U}\mathbf{x}\|_2 + (1 - \alpha) \|\mathbf{M}_{\mathbf{v}} \odot \mathbf{U}'\mathbf{x}\|_2). \quad (35)$$

Equation 34 is due to the property of ReLU activation function that $|\sigma(x)| < |x|$. The Hoeffding's inequality is used again for each row i of matrix \mathbf{U} and \mathbf{U}' with $M_{\mathbf{v},i} = 1$, and after taking a union bound, we have the following inequality with probability $1 - \frac{\delta}{k}$,

$$\|\mathbf{M}_{\mathbf{v}} \odot \mathbf{U}\mathbf{x}\|_2 = \sqrt{\sum_{M_{\mathbf{v},i}=1} |\mathbf{U}_{i,:}\mathbf{x}|^2} \quad (36)$$

$$\leq \sigma_{\mathbf{U}} \sqrt{2(h - \#\{\mathbf{M}_{\mathbf{v}} = 0\}) \log(2hk/\delta)} \|\mathbf{x}\|_2. \quad (37)$$

$\|\mathbf{M}_{\mathbf{v}} \odot \mathbf{U}'\mathbf{x}\|_2$ can be calculated similarly to Equation 37. Then after taking a union bound, with $1 - \frac{\delta}{k}$ the first term is bounded as

$$|(\mathbf{v} - \mathbf{v}')^\top \sigma(g_{\alpha}(\mathbf{x}))| \leq 2\sqrt{2} \sqrt{h - \#\{\mathbf{M}_{\mathbf{v}} = 0\}} \sigma_{\mathbf{v}} \sigma_{\mathbf{U}} \log(6hk/\delta) \|\mathbf{x}\|_2. \quad (38)$$

ii) For the **concentration upper bound** of the second term of Equation 32, we use the Hoeffding's inequality for each element of \mathbf{v} and \mathbf{v}' and take a union bound, with probability $1 - \frac{\delta}{k}$ we have the following inequality,

$$\begin{aligned} & |(\alpha \mathbf{v} + (1 - \alpha) \mathbf{v}')^\top \sigma'(g_{\alpha}(\mathbf{x}))| \\ &= |(\alpha \mathbf{v} + (1 - \alpha) \mathbf{v}')^\top \sigma'(\mathbf{y})|_{\mathbf{y}=g_{\alpha}(\mathbf{x})} \odot (\mathbf{U} - \mathbf{U}')\mathbf{x} \end{aligned} \quad (39)$$

$$\leq \sqrt{\alpha^2 + (1 - \alpha)^2} \sigma_{\mathbf{v}} \sqrt{2 \log(2k/\delta)} \|\sigma'(\mathbf{y})|_{\mathbf{y}=g_{\alpha}(\mathbf{x})} \odot (\mathbf{U} - \mathbf{U}')\mathbf{x}\|_2 \quad (40)$$

$$\leq \sigma_{\mathbf{v}} \sqrt{\log(2k/\delta)} \|(\mathbf{U} - \mathbf{U}')\mathbf{x}\|_2. \quad (41)$$

Equation 39 is due to the chain rule of differentiation and Equation 40 is due to the fact that the property $|\sigma'(\cdot)| < 1$ of the ReLU activation function. The term $\|(\mathbf{U} - \mathbf{U}')\mathbf{x}\|_2 \leq \sigma_{\mathbf{U}} \sqrt{\sum_{i=1}^h \|\mathbf{M}_{\mathbf{U},i} \odot \mathbf{x}\|_2^2} \sqrt{4 \log(2hk/\delta)}$ is obtained in

Equation 23. Then with $1 - \frac{\delta}{k}$ after taking a union bound, the second term is bounded as

$$|(\alpha \mathbf{v} + (1 - \alpha) \mathbf{v}')^\top \sigma'(g_\alpha(\mathbf{x}))| \leq 2 \log(4hk/\delta) \sigma_v \sigma_U \sqrt{\sum_{i=1}^h \|\mathbf{M}_{U,i} \odot \mathbf{x}\|_2^2}. \quad (42)$$

iii) For the **concentration upper bound** of the third term of Equation 32, first write it as

$$\left| \mathbf{v}^\top \sigma(\mathbf{U}\mathbf{x}) - \mathbf{v}'^\top \sigma(\mathbf{U}'\mathbf{x}) \right| = \left| \mathbf{v}^\top \sigma(\mathbf{U}\mathbf{x}) - \mathbf{v}^\top \sigma(\mathbf{U}'\mathbf{x}) + \mathbf{v}^\top \sigma(\mathbf{U}'\mathbf{x}) - \mathbf{v}'^\top \sigma(\mathbf{U}'\mathbf{x}) \right| \quad (43)$$

$$\leq \left| \mathbf{v}^\top [\sigma(\mathbf{U}\mathbf{x}) - \sigma(\mathbf{U}'\mathbf{x})] \right| + \left| (\mathbf{v} - \mathbf{v}')^\top \sigma(\mathbf{U}'\mathbf{x}) \right|. \quad (44)$$

Then we use the Hoeffding's inequality for each element of \mathbf{v} and \mathbf{v}' and notice that $v_i - v'_i = 0$ when $M_{v,i} = 0$. After taking a union bound, with probability $1 - \frac{\delta}{k}$ we have the following inequality,

$$\left| \mathbf{v}^\top \sigma(\mathbf{U}\mathbf{x}) - \mathbf{v}'^\top \sigma(\mathbf{U}'\mathbf{x}) \right| \leq \sigma_v \sqrt{2 \log(4k/\delta)} \|\sigma(\mathbf{U}\mathbf{x}) - \sigma(\mathbf{U}'\mathbf{x})\|_2 + \sigma_v \sqrt{4 \log(4k/\delta)} \|\mathbf{M}_v \odot \sigma(\mathbf{U}'\mathbf{x})\|_2 \quad (45)$$

$$\leq \sigma_v \sqrt{2 \log(4k/\delta)} \|(\mathbf{U} - \mathbf{U}')\mathbf{x}\|_2 + \sigma_v \sqrt{4 \log(4k/\delta)} \|\mathbf{M}_v \odot \mathbf{U}'\mathbf{x}\|_2. \quad (46)$$

Equation 46 is due to the fact the ReLU activation function $\sigma(\cdot)$ satisfied the Lipschitz continuity condition with constant 1 and $|\sigma(x)| \leq |x|$. The term $\|(\mathbf{U} - \mathbf{U}')\mathbf{x}\|_2 \leq \sigma_U \sqrt{\sum_{i=1}^h \|\mathbf{M}_{U,i} \odot \mathbf{x}\|_2^2} \sqrt{4 \log(2hk/\delta)}$ in Equation 46 can be calculated as in Equation 23 with probability $1 - \frac{\delta}{k}$ and the term $\|\mathbf{M}_v \odot \mathbf{U}'\mathbf{x}\|_2 \leq \sigma_U \sqrt{2(h - \#\{\mathbf{M}_v = 0\}) \log(2hk/\delta)} \|\mathbf{x}\|_2$ can be calculated as in Equation 37 with probability $1 - \frac{\delta}{k}$. Then take the union bound, with probability $1 - \frac{\delta}{k}$ we have

$$\left| \mathbf{v}^\top \sigma(\mathbf{U}\mathbf{x}) - \mathbf{v}'^\top \sigma(\mathbf{U}'\mathbf{x}) \right| \leq \sigma_v \sigma_U \log(8kh/\delta) (2\sqrt{2} \sqrt{\sum_{i=1}^h \|\mathbf{M}_{U,i} \odot \mathbf{x}\|_2^2} + 2\sqrt{2} \sqrt{h - \#\{\mathbf{M}_v = 0\}} \|\mathbf{x}\|_2). \quad (47)$$

In conjunction with analyses i),ii) and iii) and take a union bound choosing $k = 3$, we have with probability $1 - \delta$,

$$\begin{aligned} \left| \frac{dz_{\mathbf{x}}(\alpha)}{d\alpha} \right| &\leq \sqrt{h - \#\{\mathbf{M}_v = 0\}} 2\sqrt{2} \sigma_v \sigma_U \log(18h/\delta) \|\mathbf{x}\|_2 \\ &+ 2 \log(12h/\delta) \sigma_v \sigma_U \sqrt{\sum_{i=1}^h \|\mathbf{M}_{U,i} \odot \mathbf{x}\|_2^2} \\ &+ \sigma_v \sigma_U \log(24h/\delta) (2\sqrt{2} \sqrt{\sum_{i=1}^h \|\mathbf{M}_{U,i} \odot \mathbf{x}\|_2^2} + 2\sqrt{2} \sqrt{h - \#\{\mathbf{M}_v = 0\}} \|\mathbf{x}\|_2) \end{aligned} \quad (48)$$

$$\begin{aligned} &\leq \sqrt{h - \#\{\mathbf{M}_v = 0\}} 4\sqrt{2} \sigma_v \sigma_U \log(24h/\delta) \|\mathbf{x}\|_2 \\ &+ 4\sqrt{2} \log(24h/\delta) \sigma_v \sigma_U \sqrt{\sum_{i=1}^h \|\mathbf{M}_{U,i} \odot \mathbf{x}\|_2^2}. \end{aligned} \quad (49)$$

Then integrate them on the region \mathbb{X} . With probability $1 - \delta$ we have

$$\begin{aligned} \left| \frac{dz(\alpha)}{d\alpha} \right| &\leq \sqrt{h - \#\{\mathbf{M}_v = 0\}} 4\sqrt{2} \sigma_v \sigma_U \log(24h/\delta) \frac{db}{d+1} \\ &+ 4\sqrt{2} \sigma_v \sigma_U \log(24h/\delta) \sigma_v \sigma_U b \sqrt{\frac{d}{d+2}} \sqrt{h - \frac{\#\{\mathbf{M}_U = 0\}}{d}} \end{aligned} \quad (50)$$

$$\leq 4\sqrt{2} b \sigma_v \sigma_U \log(24h/\delta) (\sqrt{h - \#\{\mathbf{M}_v = 0\}} + \sqrt{h - \frac{\#\{\mathbf{M}_U = 0\}}{d}}) \quad (51)$$

$$= 4\sqrt{2} b \sigma_v \sigma_U \sqrt{h} \log(24h/\delta) (\sqrt{1 - \rho_v} + \sqrt{1 - \rho_M}). \quad (52)$$

Equation 50 is due to the integration $\frac{1}{|\mathbb{X}|} \int_{\mathbb{X}} \|\mathbf{x}\|_2 d\mathbf{x} = \frac{db}{d+1}$ and $\frac{1}{|\mathbb{X}|} \int_{\mathbb{X}} \sqrt{\sum_{i=1}^h \|\mathbf{M}_{\mathbf{U},i} \odot \mathbf{x}\|_2^2} d\mathbf{x} \leq \sqrt{(h - \frac{\#\{\mathbf{M}_{\mathbf{U}}=0\}}{d}) \frac{db^2}{d+2}}$ from Equation 31

3) For the second derivative, we have

$$\left| \frac{d^2 z_{\mathbf{x}}(\alpha)}{d\alpha^2} \right| \leq 2 |(\mathbf{v} - \mathbf{v}')^\top \sigma'(g_{\alpha}(\mathbf{x}))| + |(\alpha \mathbf{v} + (1 - \alpha) \mathbf{v}')^\top \sigma''(g_{\alpha}(\mathbf{x}))|. \quad (53)$$

i) For the **concentration upper bound** of the first term of Equation 53, we use the Hoeffding's inequality for each element of $\mathbf{v} - \mathbf{v}'$ and notice that $v_i - v'_i = 0$ when $M_{v,i} = 0$, with probability $1 - \frac{\delta}{k}$, we have

$$2 |(\mathbf{v} - \mathbf{v}')^\top \sigma'(g_{\alpha}(\mathbf{x}))| = 2 |(\mathbf{v} - \mathbf{v}')^\top \sigma'(\mathbf{y})|_{\mathbf{y}=g_{\alpha}(\mathbf{x})} \odot (\mathbf{U} - \mathbf{U}') \mathbf{x}| \quad (54)$$

$$= 2 |(\mathbf{v} - \mathbf{v}')^\top \mathbf{M}_{\mathbf{v}} \odot \sigma'(\mathbf{y})|_{\mathbf{y}=g_{\alpha}(\mathbf{x})} \odot (\mathbf{U} - \mathbf{U}') \mathbf{x}| \quad (55)$$

$$\leq 4\sigma_v \sqrt{\log(2k/\delta)} \|\mathbf{M}_{\mathbf{v}} \odot \sigma'(\mathbf{y})|_{\mathbf{y}=g_{\alpha}(\mathbf{x})} \odot (\mathbf{U} - \mathbf{U}') \mathbf{x}\|_2 \quad (56)$$

$$\leq 4\sigma_v \sqrt{\log(2k/\delta)} \|\mathbf{M}_{\mathbf{v}} \odot (\mathbf{U} - \mathbf{U}') \mathbf{x}\|_2. \quad (57)$$

Equation 54 is due to the chaine rule of differentiation, Equation 55 is due to $v_i = v'_i$ when $M_{v,i} = 0$, Equation 56 is due to Hoeffding's inequation and Equation 57 is due to the property $|\sigma'(x)| < 1$ of the ReLU activation function. For the item $\|\mathbf{M}_{\mathbf{v}} \odot (\mathbf{U} - \mathbf{U}') \mathbf{x}\|_2$, notice that $U_{ij} = U'_{ij}$ when $M_{U,ij} = 0$ and take a union bound with probability $1 - \frac{\delta}{k}$, we have

$$\|\mathbf{M}_{\mathbf{v}} \odot (\mathbf{U} - \mathbf{U}') \mathbf{x}\|_2 \leq \sqrt{\sum_{M_{v,i}=1} \|\mathbf{M}_{\mathbf{U},i} \odot (\mathbf{U}_{i,:} - \mathbf{U}'_{i,:}) \mathbf{x}\|^2} \quad (58)$$

$$\leq \sqrt{\sum_{M_{v,i}=1} |(\mathbf{U}_{i,:} - \mathbf{U}'_{i,:}) (\mathbf{M}_{\mathbf{U},i} \odot \mathbf{x})|^2} \quad (59)$$

$$\leq \sigma_U \sqrt{\sum_{M_{v,i}=1} \|\mathbf{M}_{\mathbf{U},i} \odot \mathbf{x}\|_2^2} \sqrt{4 \log(2hk/\delta)}. \quad (60)$$

Then with $1 - \frac{\delta}{k}$ after taking a union bound, the first term is bounded as

$$2 |(\mathbf{v} - \mathbf{v}')^\top \sigma'(g_{\alpha}(\mathbf{x}))| \leq 8\sigma_v \sigma_U \log(4hk/\delta) \sqrt{\sum_{M_{v,i}=1} \|\mathbf{M}_{\mathbf{U},i} \odot \mathbf{x}\|_2^2}. \quad (61)$$

ii) For the **concentration upper bound** of the second term of Equation 53, note that property $\sigma''(x) = 0$ of ReLU activation function, then

$$\begin{aligned} & |(\alpha \mathbf{v} + (1 - \alpha) \mathbf{v}')^\top \sigma''(g_{\alpha}(\mathbf{x}))| \\ &= |(\alpha \mathbf{v} + (1 - \alpha) \mathbf{v}')^\top \sigma''(\mathbf{y})|_{\mathbf{y}=g_{\alpha}(\mathbf{x})} \odot (\mathbf{U} - \mathbf{U}') \mathbf{x} \odot (\mathbf{U} - \mathbf{U}') \mathbf{x}| \end{aligned} \quad (62)$$

$$= 0. \quad (63)$$

In conjunction with analyses i) and ii) and take a union bound choosing $k = 1$, with probability $1 - \delta$ we have

$$\left| \frac{d^2 z_{\mathbf{x}}(\alpha)}{d\alpha^2} \right| \leq 8\sigma_v \sigma_U \log(4h/\delta) \sqrt{\sum_{M_{v,i}=1} \|\mathbf{M}_{\mathbf{U},i} \odot \mathbf{x}\|_2^2}. \quad (64)$$

Then integrate them on the region \mathbb{X} . With probability $1 - \delta$ we have

$$\left| \frac{d^2 z(\alpha)}{d\alpha^2} \right| \leq 8\sigma_v \sigma_U \log(4h/\delta) \sqrt{(h - \frac{\max\{\#\{\mathbf{M}_{\mathbf{U}}=0\}, d\#\{\mathbf{M}_{\mathbf{v}}=0\}\}}{d}) \frac{db^2}{d+2}} \quad (65)$$

$$\leq 8\sigma_v \sigma_U \log(4h/\delta) b \sqrt{(h - \frac{\max\{hd\rho_U, hd\rho_v\}}{d})} \quad (66)$$

$$\leq 8\sigma_v \sigma_U \log(4h/\delta) b \sqrt{h} \sqrt{(1 - \max\{\rho_U, \rho_v\})}. \quad (67)$$

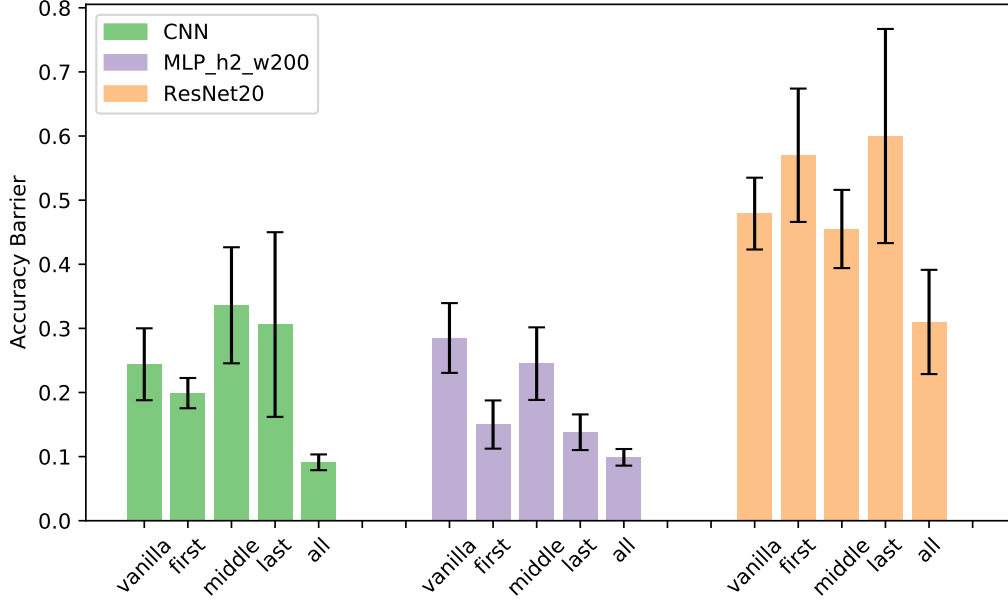


Figure 5: **Layer-wise analysis of TNA-PFN.** The dataset is CIFAR-10. “vanilla” refers to vanilla training. “first”/“middle”/“last” refers to only applying TNA-PFN to the first/middle/last layer. “all” refers to applying TNA-PFN to all layers (vanilla TNA-PFN). For CNN, the first layer is the convolution layer Conv2d(3, 32, 3), the middle layer is the convolution layer Conv2d(64, 64, 3), and the last layer is the fully connected layer Linear(64, 10) for classification; for MLP_h2_w200, the first layer is the fully connected layer Linear(32*32*3, 200), the middle layer is the fully connected layer Linear(200, 200), and the last layer is the fully connected layer Linear(200, 10) for classification; for ResNet20, the first layer is the convolution layer Conv2d(3, 16, kernel_size=3, stride=1, padding=1, bias=False), the middle layer is the middle block, and the last layer is the fully connected layer Linear(64*block.expansion, 10) for classification;

Equation 65 is due to the integration $\frac{1}{|\mathbb{X}|} \int_{\mathbb{X}} \sqrt{\sum_{i=1}^h \|M_{U,i} \odot \mathbf{x}\|_2^2} d\mathbf{x}$ satisfying

$$\frac{1}{|\mathbb{X}|} \int_{\mathbb{X}} \sqrt{\sum_{M_{v,i}=1} \|M_{U,i} \odot \mathbf{x}\|_2^2} d\mathbf{x} \leq \sqrt{\left(\frac{1}{|\mathbb{X}|} \int_{\mathbb{X}} \sum_{M_{v,i}=1} \|M_{U,i} \odot \mathbf{x}\|_2^2 d\mathbf{x}\right) \left(\frac{1}{|\mathbb{X}|} \int_{\mathbb{X}} d\mathbf{x}\right)} \quad (68)$$

$$= \sqrt{\frac{1}{|\mathbb{X}|} \int_{\mathbb{X}} \#\{M_U \odot M_V = 1\} x_i^2 d\mathbf{x}} \quad (69)$$

$$= \sqrt{\frac{\#\{M_U \odot M_V = 1\}}{d} \frac{1}{|\mathbb{X}|} \int_{\mathbb{X}} \|\mathbf{x}\|_2^2 d\mathbf{x}} \quad (70)$$

$$\leq \sqrt{\left(h - \frac{\max\{\#\{M_U = 0\}, d\#\{M_V = 0\}\}}{d}\right) \frac{db^2}{d+2}}, \quad (71)$$

where M_V is the matrix whose each column is M_v . Equation 68 is due to Cauchy-Schwarz inequality of integration, Equation 69 and Equation 70 is due to the symmetry of different components of \mathbf{x} and Equation 71 is due to the integration $\frac{1}{|\mathbb{X}|} \int_{\mathbb{X}} \|\mathbf{x}\|_2^2 d\mathbf{x} = \frac{db^2}{d+2}$ and $\#\{M_U \odot M_V = 1\} \leq \min\{\#\{M_U = 1\}, \#\{M_V = 1\}\} = \min\{\#\{M_U = 1\}, d\#\{M_v = 1\}\}$. \square

C. More Analysis and Results

C.1. More Results and Illustrations in Linear Mode Connectivity

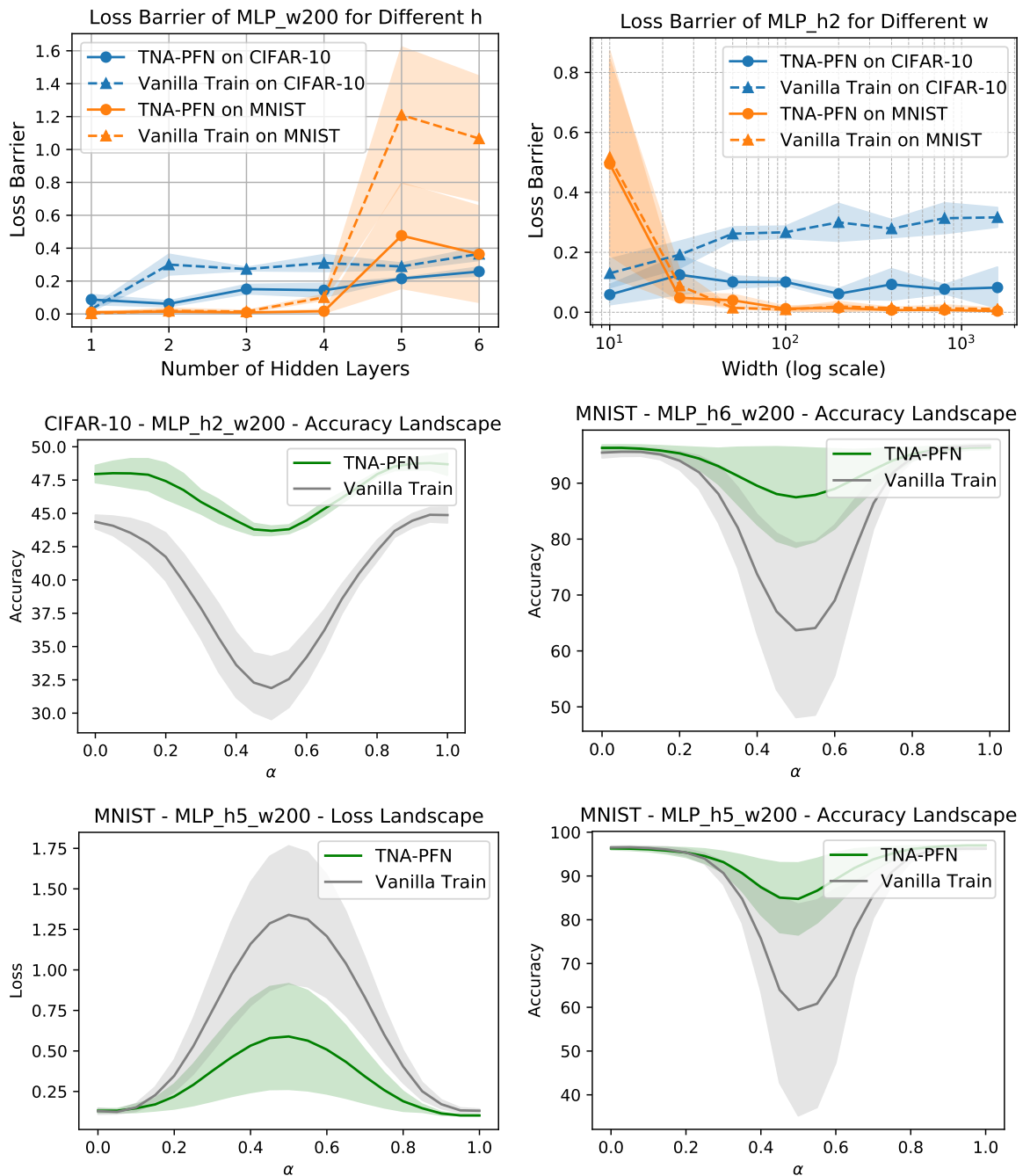


Figure 6: **Upper two: Loss barriers of MLP under different hidden layers (h) and widths (w). Middle two and Lower two: Accuracy and loss landscapes of MLPs.**

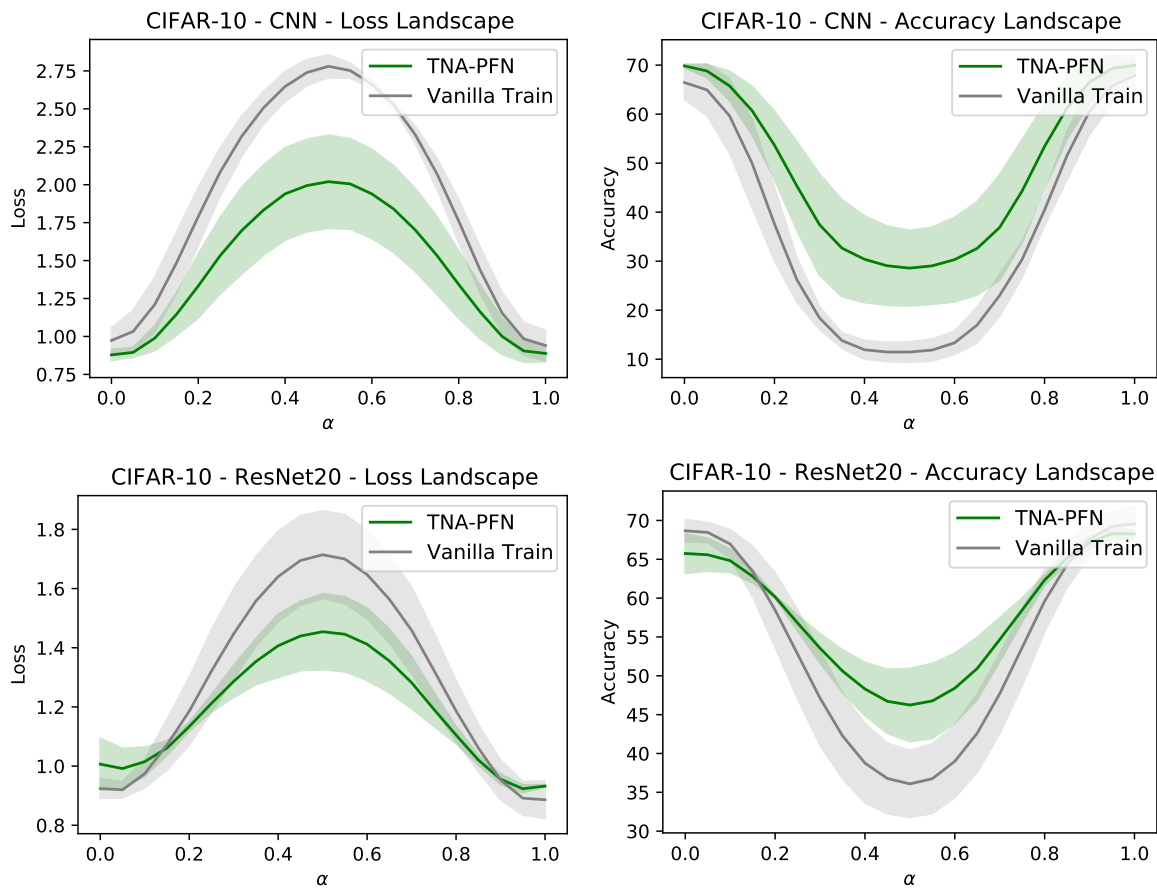


Figure 7: **Upper two: Loss and accuracy landscapes of CNN. Lower two: Loss and accuracy landscapes of ResNet20.**

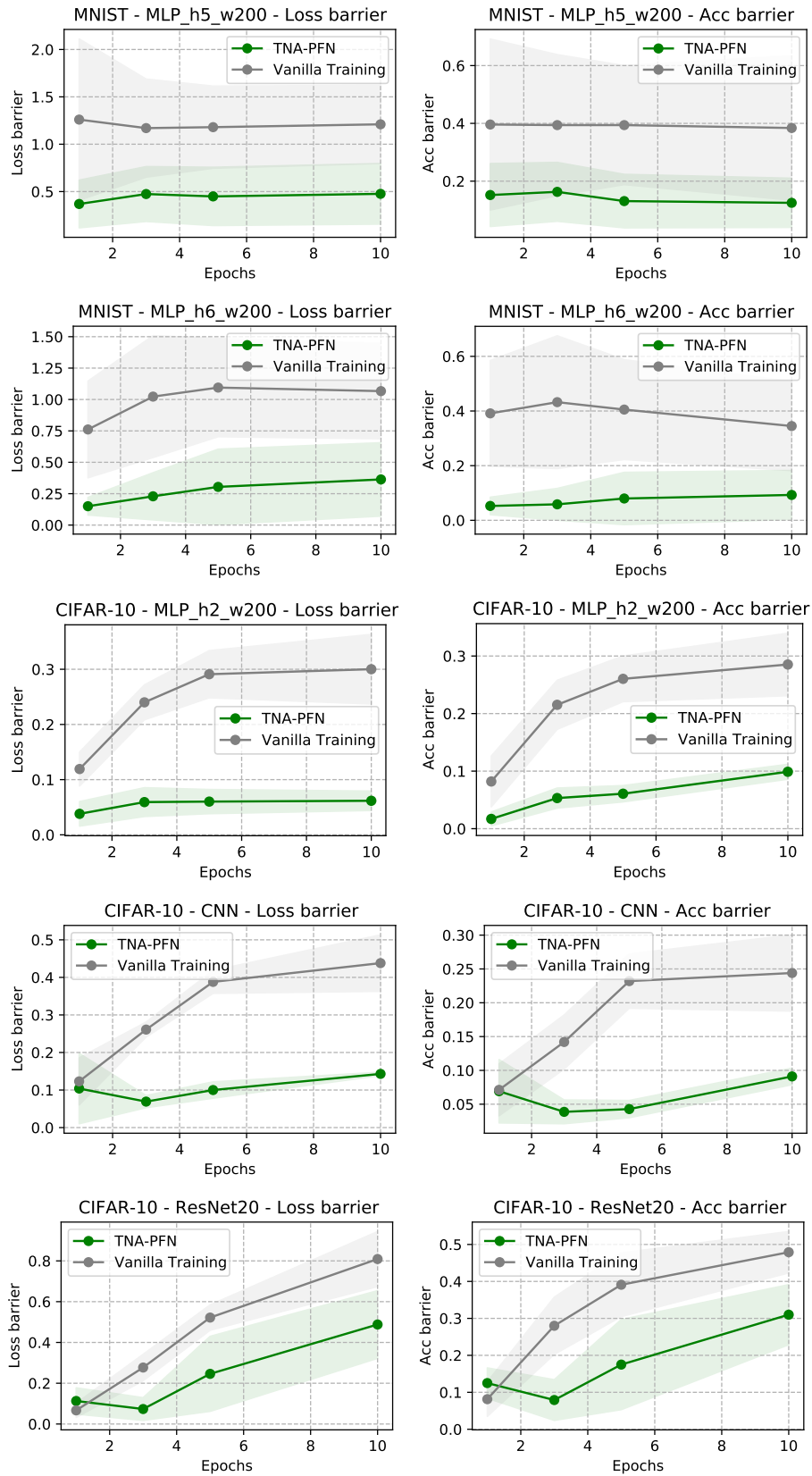


Figure 8: Barrier changes during training for different datasets and models.

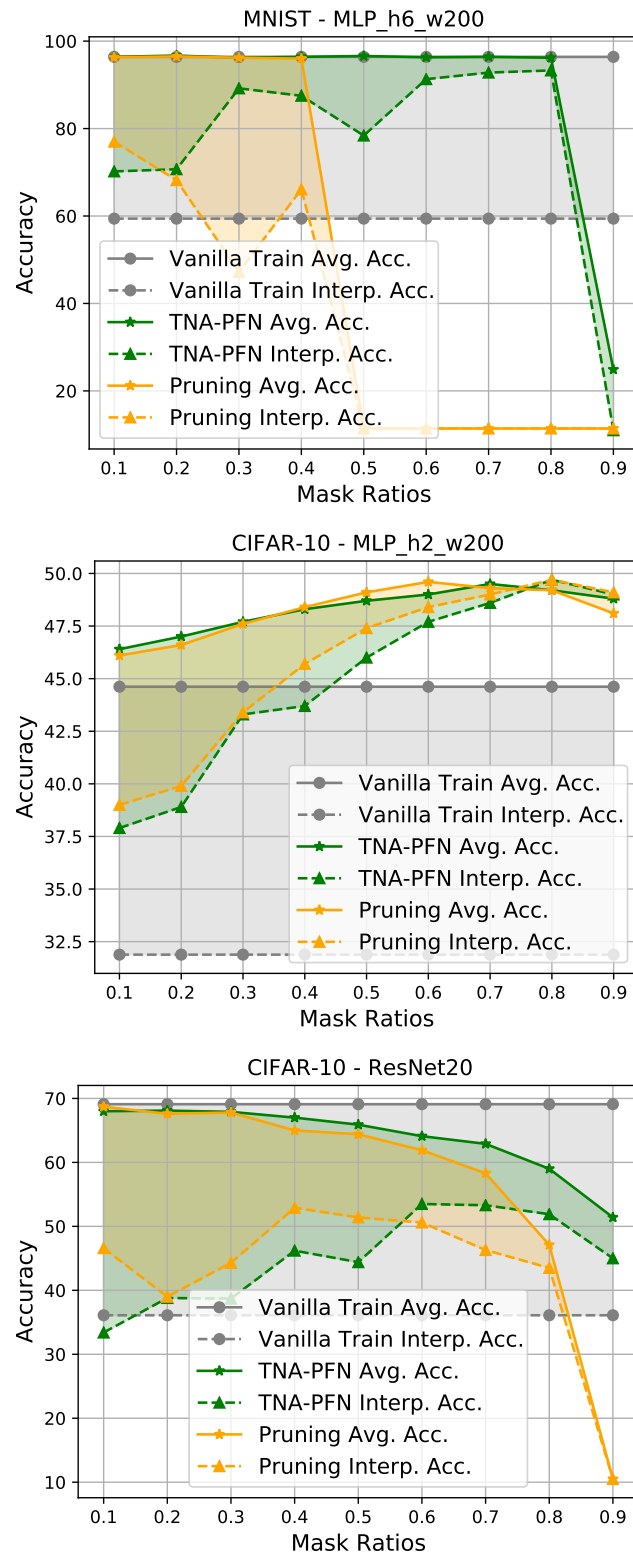


Figure 9: **More results about pruning and TNA-PFN under different mask ratios.** The shadow areas mean the accuracy barriers.

Results on large-scale dataset. We conduct experiments on Tiny ImageNet (tin, Accessed: 2023), a subset of ImageNet (Deng et al., 2009), containing 100000 images of 200 classes (500 for each class) downsized to 64×64 colored images. Each class has 500 training images, 50 validation images, and 50 test images. The result is shown in Table 10. It can be seen that under large-scale datasets, TNA-PFN also can reduce the barriers in the linear mode connectivity.

Layer-wise analysis. We conduct a layer-wise analysis of TNA-PFN to see which layer matters most in improving LMC in Figure 5, and different model architecture poses different results. For simple CNN, only applying neuron fixing in the first layer (convolution) will improve LMC, and partially fixing weights in the middle (convolution) and the last (fully connected) layers will cause barrier increases. For MLP_h2_w200, we observe that independently fixing one layer will all cause barrier reductions, and the performance is more dominant when fixing the first and the last layers; jointly fixing all layers (“all”) will have the lowest barrier. For ResNet20, it is revealed that only fixing the middle layers (the middle block) will cause barrier degradation.

Extensions of Figure 3. We provide more illustrations about the loss and accuracy barriers and landscapes in Figure 6.

Extensions of Figure 4. We provide illustrations about the loss and accuracy barriers of the Figure 4 results in Figure 7. It is obvious that TNA-PFN can lower the barriers in LMC.

Loss and accuracy barriers w.r.t. epochs. We demonstrate the barrier changes during training in Figure 8. It is shown that barriers increase during training, revealing that two independent networks diverge in parameter space. TNA-PFN has slower barrier-increasing rates than vanilla training.

Extensions of Figure 2. We provide more results about pruning and TNA-PFN under different mask ratios in Figure 9. Interestingly, for CNN, pruning and TNA-PFN improve both the accuracy and connectivity and the improvements go up along with the ratio increasing. On the other side, we observe an obvious accuracy-connectivity tradeoff for ResNet20 and it is more severe for pruning. Also, considering the layer-wise evaluation for ResNet in Figure 5, we reckon it is important to devise different mask strategies for the layers in ResNet and other deeper or more complex models.

C.2. More Results and Illustrations in Federated Learning

Different local epochs. We verify the TNA variants in FL under different local epochs in Figure 11. We find that the improvements are also strong when there are more local updates. It is observed that FedPNU is more robust regarding local epochs, and this is because it learns in the complementary subspaces progressively, reducing the negative effects of subspaces on accuracy. Similar reasons are also for why FedPNU is robust when the mask ratio is as high as 0.9 in Figure 12.

The effects of mask ratios for FedPFN and FedPNU. From Figure 12, it is shown that FedPFN benefits under smaller subspaces (higher mask ratios) but falls short when the subspace is too small (ratio $\rho = 0.9$); whereas FedPNU is robust across all mask ratios due to its progressive learning.

Extensions of Figure 12. We show the performances of FedPFN and FedPNU under different mask ratios for ResNet20 in Figure 10. The results indicate that FedPFN is sensitive to the mask ratio while FedPNU is more robust. FedPNU reaches higher performances under higher mask ratios ($\rho \in [0.8, 0.9]$).

Illustrations of the learning curves. We present the test accuracy curves of FedAvg, FedPFN, and FedPNU in Figure 13. Our methods show dominant advantages over FedAvg in both IID and non-IID settings, especially for the more complex datasets, CIFAR-10 and CIFAR-100.

Table 10: **Linear mode connectivity on Tiny ImageNet.** The ρ for CNN is 0.4 and the ρ for ResNet18 is 0.3. The learning rate is 0.08.

Models	Metrics	Vanilla Train	TNA-PFN
CNN	Avg. Acc.	9.85±0.3	11.4±0.6
	Interp. Acc.	1.4±0.2	2.91±0.9
	Acc. Barrier	0.86±0.03	0.75±0.07 (12.8%↓)
	Loss Barrier	0.84±0.08	0.75±0.09 (10.4%↓)
ResNet20	Avg. Acc.	31.8±0.3	31.6±0.4
	Interp. Acc.	6.86±1.8	12.5±2.1
	Acc. Barrier	0.78±0.06	0.60±0.07 (23%↓)
	Loss Barrier	1.6±0.2	1.2±0.09 (22.2%↓)

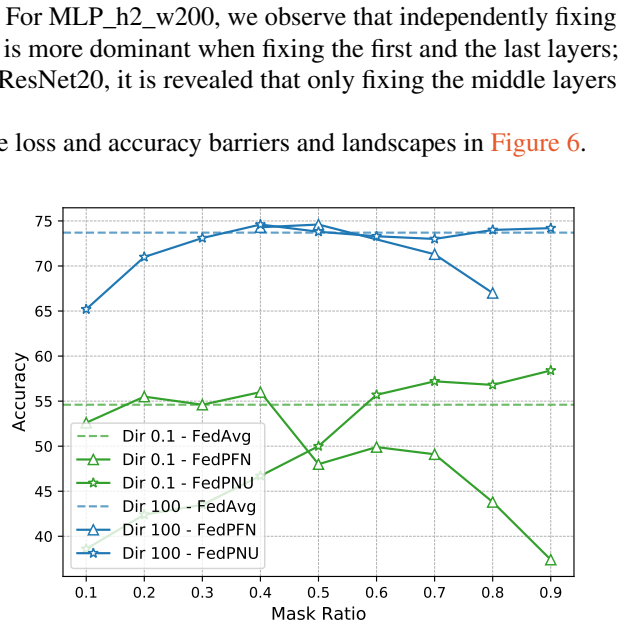


Figure 10: **Performances of FedPFN and FedPNU under different mask ratios.** CIFAR-10, ResNet20, and $E = 3$.

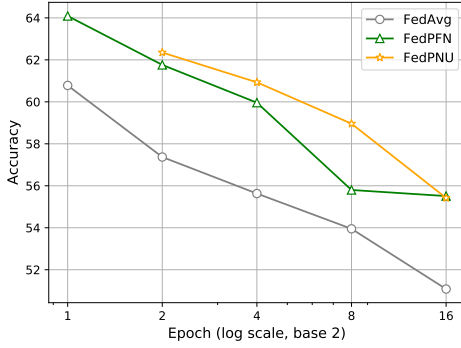


Figure 11: **Performances of FedPFN and FedPNU under different local epochs.** CIFAR-10 with $\text{dir} = 0.1$ and the model is CNN.

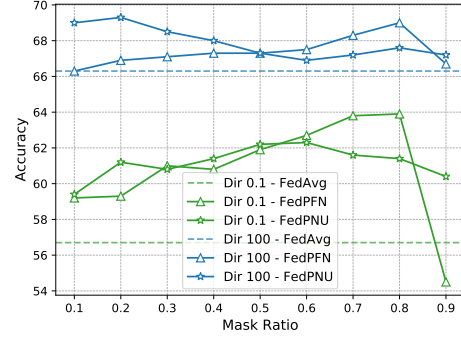


Figure 12: **Performances of FedPFN and FedPNU under different mask ratios.** CIFAR-10, CNN, and $E = 3$.

C.3. Model soup analysis

We show the model soup results of pruning and TNA-PFN under different mask ratios in Figure 14. Interestingly, for TNA-PFN, we find when the mask ratios increase, the individual accuracies also increase, while the greedy soup accuracy may drop under a large ρ . For pruning, the generalization is terrible since pruning destroys the intrinsic network representations of the pretrained models.

D. Preliminary of Federated Learning

Federated learning usually involves a server and n clients to jointly learn a global model without data sharing, which is originally proposed in (McMahan et al., 2017). Denote the set of clients by \mathcal{S} , the labeled data of client i by $\mathcal{D}_i = \{(x_j, y_j)\}_{j=1}^{N_i}$, and the parameters of the current global model by \mathbf{w}_g^t . FL starts with **client training** in parallel, initializing each clients' model \mathbf{w}_i^t with \mathbf{w}_g^t .

FL is more communication-efficient than conventional distributed training, in that it assumes the clients train the models for epochs (the full data) instead of iterations (the mini-batch data) between the communications to the server. **The number of local epochs is denoted as E .**

In each local epoch, clients conduct SGD update with a local learning rate η_l , each SGD iteration shows as

$$\text{Client training:} \quad \mathbf{w}_i^t \leftarrow \mathbf{w}_i^t - \eta_l \nabla \ell(B_k, \mathbf{w}_i^t), \text{ for } k = 1, 2, \dots, K, \quad (72)$$

where ℓ is the loss function and B_k is the mini-batch sampled from \mathcal{D}_i at the k th iteration. After the client local updates, the server samples m clients for aggregation. The client i 's pseudo gradient of local updates is denoted as $\mathbf{g}_i^t = \mathbf{w}_g^t - \mathbf{w}_i^t$. Then, the server conducts FEDAVG to aggregate the local updates into a new global model.

$$\text{Weighted Model aggregation:} \quad \mathbf{w}_g^{t+1} = \mathbf{w}_g^t - \sum_{i=1}^m \lambda_i \mathbf{g}_i^t, \quad \lambda_i = \frac{|\mathcal{D}_i|}{|\mathcal{D}|}, \forall i \in [m]. \quad (73)$$

With the updated global model \mathbf{w}_g^{t+1} , it then starts the next round of **client training**. The procedure of FL, therefore iterates between Equation 72 and Equation 73, for T communication rounds.

We assume the sum of clients' data as $\mathcal{D} = \bigcup_{i \in \mathcal{S}} \mathcal{D}_i$. The IID data distributions of clients refer to each client's distribution \mathcal{D}_i is IID sampled from \mathcal{D} . However, in practical FL scenarios, **heterogeneity** exists among clients that their data are **non-IID** with each other. Each client may have different data distributions in the input (e.g. image distribution) or output (e.g. label distribution).

E. More Discussions about Related Works

In this section, we give a more detailed discussion of the related works.

Linear Mode Connectivity. Linear mode connectivity refers to the phenomenon that there exists a loss (energy) barrier along the linear interpolation path of two networks, in the cases where i) the two networks have the same initialization and are

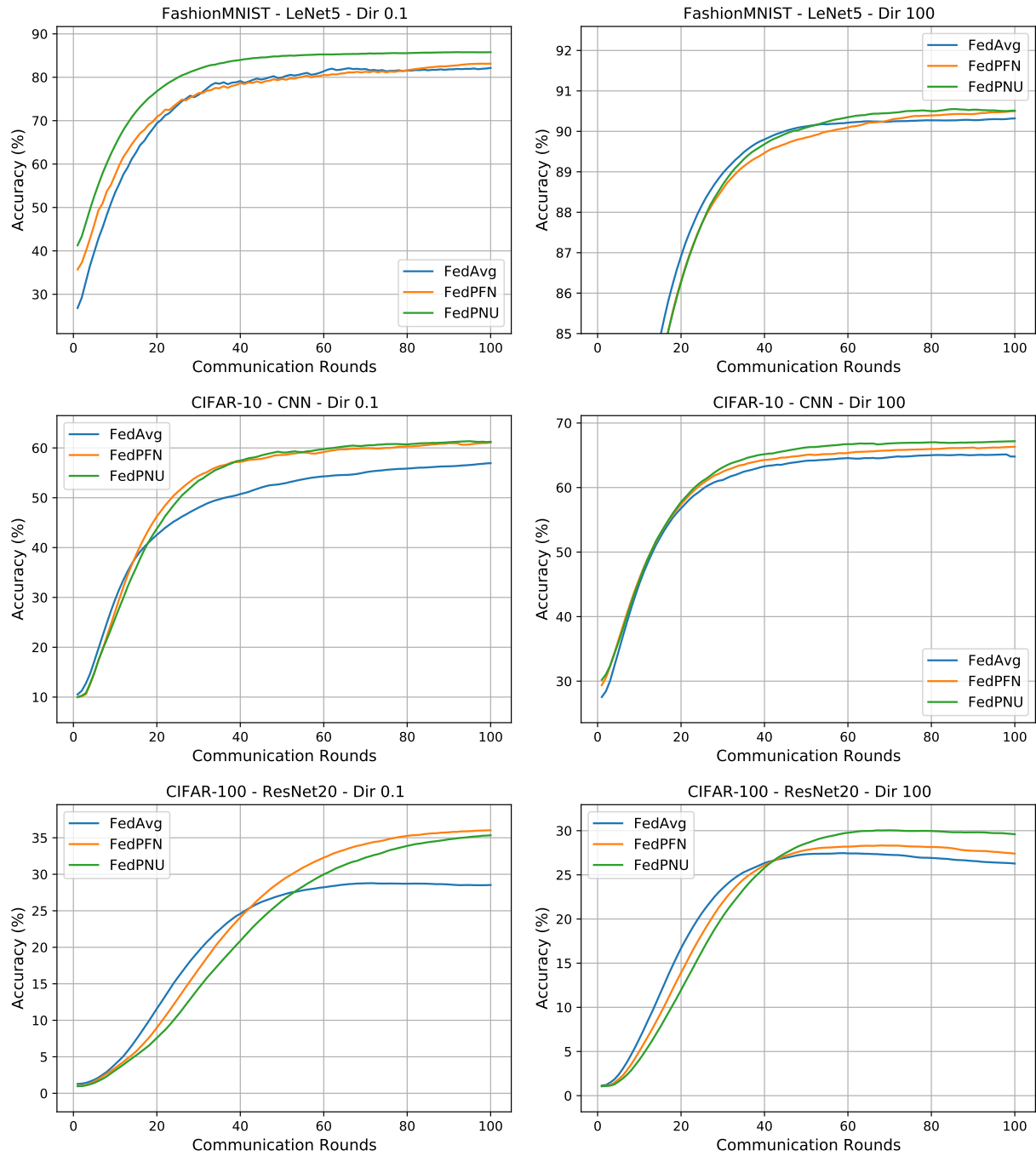


Figure 13: Test accuracy curves of the federated learning methods.

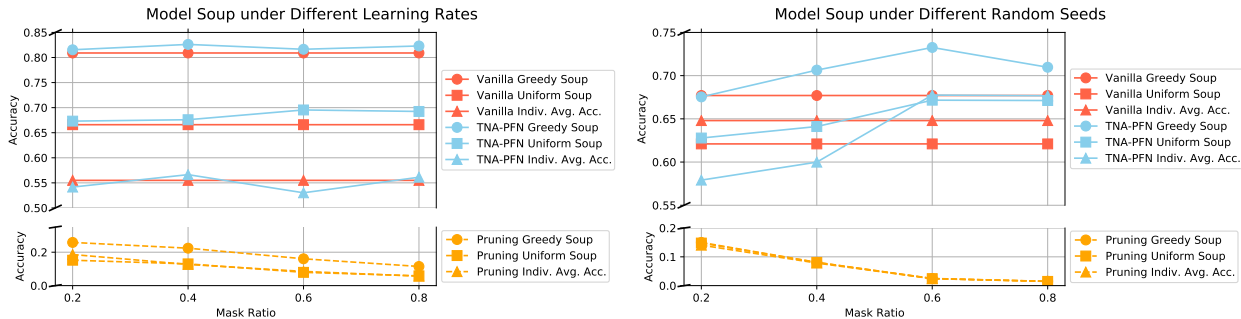


Figure 14: Results of model soup under different mask ratios. The initialization is ViT-B/32 and the finetuned dataset is CIFAR-100.

trained on the same dataset but with different random seeds (data shuffles and augmentations) (Ainsworth et al., 2022); ii) the two networks are with different initializations but are trained on the same dataset (Entezari et al., 2022); iii) the two networks are the initial network and the final trained network (Vlaar & Frankle, 2022). Specifically, Adilova et al. (2023) examines the linear mode connectivity of different layers. Vlaar & Frankle (2022) studies the relationship between generalization and the initial-to-final linear mode connectivity. Frankle et al. (2020) connects linear mode connectivity with the lottery ticket hypothesis and finds better connectivity can result in better pruning performances. Zhao et al. (2020) bridges mode connectivity and adversarial robustness. Some works try to extend mode connectivity beyond “linear”, e.g., searching for a non-linear low-loss path (Draxler et al., 2018) or studying mode connectivity under spurious attributes (Lubana et al., 2023).

Permutation Invariance and Model Fusion. Permutation invariance (a.k.a. permutation symmetry) refers to the property of neural networks that the positions of neurons can be permuted without changing its function (Simsek et al., 2021; Hecht-Nielsen, 1990), and it is believed to be the primary cause of loss barrier in linear mode connectivity (Entezari et al., 2022; Ainsworth et al., 2022). Entezari et al. (2022) hypothesizes that if taking the permutation invariance into consideration, all solutions can be mapped into the same low-loss basin with connectivity. Further, Ainsworth et al. (2022) validates this hypothesis by using “re-basin” which aims to find the appropriate permutation matrices to map the networks into the same basin. Other methods are also utilized to match the neurons for better model fusion, such as optimal transport (Singh & Jaggi, 2020), Bayesian nonparametric technique (Yurochkin et al., 2019; Wang et al., 2020a), Hungarian algorithm (Tatro et al., 2020), graph matching (Liu et al., 2022a), and implicit Sinkhorn differentiation (Peña et al., 2023). We note that all these methods are for post-matching after training, while we focus on training-time neuron alignment. Note that the previous work of PAN (Li et al., 2022) shares a similar motivation with ours. PAN uses position-aware encoding for intermediate activations, which is orthogonal to our methods, and it only focuses on FL, while we study both LMC and model fusion in FL.

Relation with Frankle et al. (2020). In Frankle et al. (2020), the authors use linear mode connectivity to study the performances of lottery-ticket-hypothesis-based pruning and find that the sparse pruned model with good connectivity will be more likely to reach the full accuracy after pruning. While in this paper, we find random pruning (not necessarily lottery tickets) can improve linear mode connectivity. Though the two papers both discuss the relationship between pruning and linear mode connectivity, they have different focuses and contributions: Frankle et al. (2020) finds LMC indicates better results of pruning, whereas we find pruning can improve LMC, and the causal logic is different.

Subspace Learning. Subspace learning has various forms, and we summarize other forms of subspaces that have not appeared in this paper. Intrinsic dimensions use a random low-rank matrix to map the network parameters into a subspace and it finds neural networks have lower intrinsic dimensions than the original dimension to reach a close or same accuracy (Li et al., 2018a). Further, LoRA introduces intrinsic dimension in parameter-efficient finetuning of large language models (Hu et al., 2021); and Gressmann et al. (2020) improves learning in intrinsic dimensions above random matrices. Additionally, subspaces are used in improving continual and incremental learning. Chaudhry et al. (2020) use a projection matrix to map the features into orthogonal subspaces to prevent catastrophic forgetting in continual learning; Akyurek et al. (2021) adds a subspace regularizer for improving few-shot class incremental learning.

Subspace and Partial Training in Federated Learning. Previous works in federated learning apply subspace or partial training methods, but they have different motivations and are orthogonal to our approaches FedPFN and FedPNU. In Isik et al. (2022), the authors propose to train a mask on a random network instead of training the neurons from communication efficiency, while in Li et al. (2021), it is proposed to learn a personalized sparsened network at clients. Additionally, partial training is adopted in federated learning to save computation and communication. Lee et al. (2023) proposes to train $\frac{1}{E}$ part of models and then aggregate on the server to relieve the negative effects brought by large local epochs. Yang et al. (2022)

proposes each client train $\frac{1}{n}$ disjoint part of the whole model and combines the model on the server for efficiency. [Niu et al. \(2022\)](#) aims to enable large-model training at edges by decoupling the model into several principle sub-models. In [Hahn et al. \(2022\)](#), the authors utilize linear mode connectivity to improve personalization in federated learning.

Loss Landscape of Neural Networks and Generalization. Deep neural networks (DNNs) are highly non-convex and over-parameterized, and visualizing the loss landscape of DNNs ([Li et al., 2018b](#); [Vlaar & Frankle, 2022](#)) helps understand the training process and the properties of minima. There are mainly two lines of works about the loss landscape of DNNs. The first one is the linear interpolation of neural network loss landscape ([Vlaar & Frankle, 2022](#); [Garipov et al., 2018](#); [Draxler et al., 2018](#)), it plots linear slices of the landscape between two networks. In linear interpolation loss landscape, mode connectivity ([Draxler et al., 2018](#); [Vlaar & Frankle, 2022](#); [Entezari et al., 2022](#)) is referred to as the phenomenon that there might be increasing loss on the linear path between two minima found by SGD, and the loss increase on the path between two minima is referred to as (energy) barrier. It is also found that there may exist barriers between the initial model and the trained model ([Vlaar & Frankle, 2022](#)). The second line concerns the loss landscape around a trained model’s parameters ([Li et al., 2018b](#)). It is shown that the flatness of loss landscape curvature can reflect the generalization ([Foret et al., 2020](#); [Izmailov et al., 2018](#)) and top hessian eigenvalues can present flatness ([Yao et al., 2020](#); [Jastrzębski et al., 2018](#)). Networks with small top hessian eigenvalues have flat curvature and generalize well. Previous works seek flatter minima for improving generalization by implicitly regularizing the hessian ([Foret et al., 2020](#); [Kwon et al., 2021](#); [Du et al., 2021](#)).